



Ecoresorbable and bioresorbable microelectromechanical systems

Quansan Yang ^{ID 1,2}, Tzu-Li Liu^{1,2}, Yeguang Xue², Heling Wang ^{ID 2}, Yameng Xu^{3,4}, Bashar Emon⁵, Mingzheng Wu ^{ID 6}, Corey Rountree⁷, Tong Wei⁸, Irawati Kandela^{9,10}, Chad R. Haney ^{ID 10,11,12}, Anil Brikha^{10,11}, Iwona Stepien^{9,10}, Jessica Hornick¹³, Rebecca A. Sponenburg¹⁴, Christina Cheng ^{ID 15}, Lauren Ladehoff¹⁶, Yitong Chen¹⁷, Ziyang Hu¹, Changsheng Wu¹, Mengdi Han¹, John M. Torkelson^{3,8}, Yevgenia Kozorovitskiy ^{ID 6,10}, M. Taher A. Saif^{5,18}, Yonggang Huang ^{ID 2,3,19}, Jan-Kai Chang ^{ID 1,20}✉ and John A. Rogers ^{ID 1,2,3,12,21}✉

Microelectromechanical systems (MEMS) are essential components in many electronic technologies for consumer and industrial applications. Such devices are typically made using materials selected to support long operational lifetimes, but MEMS designed to physically disintegrate or to dissolve after a targeted period could provide a route to reduce electronic waste and could enable applications that require a finite operating timeframe, such as temporary medical implants. Here we report ecoresorbable and bioresorbable MEMS that are based on fully water-soluble material platforms and can either naturally resorb into the environment to eliminate solid waste or in the body to avoid a need for surgical extraction. We illustrate the biocompatibility of the approach with mechanobiology, histology and haematology studies of the implanted devices and their dissolution end products. We also demonstrate bioresorbable encapsulating materials and deployment strategies in small animal models to reduce device damage, confine mobile fragments and provide robust adhesion with adjacent tissues.

Micro-electromechanical systems (MEMS) are critical components in many technologies^{1–12}, including inertial sensors, acoustic microphones, and electrostatic or thermal actuators. The mobile device industry has, for instance, an estimated global annual production of 30 billion MEMS components^{13–15}. Conventional MEMS devices are engineered to exhibit reliable operation and long-term stability for a range of conditions. However, MEMS devices that behave in a transient manner—supporting stable operation for a finite period of time, followed by physical disintegration, chemical dissolution or enzymatic degradation—could be of interest for a range of technologies. Ecoresorbable devices that can breakdown into non-toxic and dissolvable constituents reduce the need for solid waste associated with discarded consumer devices in the world^{16–20}. Such devices are of particular relevance to MEMS components because of the prevalence of electronic technologies that contain MEMS and the short cycle times between different technology generations^{21,22}. Alternatively, bioresorbable devices used in biomedical implants for temporary medical conditions could lower the risks of infection²³ and complications from surgical retrieval required

with permanent devices^{24,25}. There has been much recent work on transient electronics^{26–31}, but developments in transient MEMS that exhibit ecoresorbable and bioresorbable functionality remain limited.

In this Article, we report ecoresorbable and bioresorbable MEMS (eb-MEMS) devices, as well as encapsulation strategies for their safe and effective biointegration. We explore the material chemistry and engineering design choices for eb-MEMS for several device types including electrocapacitive sensors, electrostatic actuators and electrothermal actuators. We report materials, fabrication methods and encapsulation strategies for eb-MEMS, and demonstrate schemes for integration with mechanically flexible substrates and with biodegradable integrated circuits. We investigate the biocompatibility of eb-MEMS before and after dissolution through mechanobiology, histology and haematology studies, the results of which suggest that these technologies can be safely used in biointegrated systems. In vitro and in vivo experiments, including the insertion of an eb-MEMS device in rat dorsal subcutaneous tissue, illustrate the use of our eb-MEMS in temporary implants. We also show that the encapsulation materials and associated deployment strategies can

¹Querrey Simpson Institute for Bioelectronics, Northwestern University, Evanston, IL, USA. ²Department of Mechanical Engineering, Northwestern University, Evanston, IL, USA. ³Department of Materials Science and Engineering, Northwestern University, Evanston, IL, USA. ⁴The Institute of Materials Science and Engineering, Washington University in St. Louis, St. Louis, MO, USA. ⁵Department of Mechanical Science and Engineering, University of Illinois at Urbana-Champaign, Urbana, IL, USA. ⁶Department of Neurobiology, Northwestern University, Evanston, IL, USA. ⁷Department of Mechanical and Industrial Engineering, University of Illinois at Chicago, Chicago, IL, USA. ⁸Department of Chemical and Biological Engineering, Northwestern University, Evanston, IL, USA. ⁹Developmental Therapeutics Core, Northwestern University, Evanston, IL, USA. ¹⁰Chemistry Life Processes Institute, Northwestern University, Evanston, IL, USA. ¹¹Center for Advanced Molecular Imaging, Northwestern University, Evanston, IL, USA. ¹²Department of Biomedical Engineering, Northwestern University, Evanston, IL, USA. ¹³Biological Imaging Facility, Northwestern University, Evanston, IL, USA. ¹⁴Quantitative Bio-element Imaging Center, Northwestern University, Evanston, IL, USA. ¹⁵Department of Materials Science and Engineering, Stanford University, Stanford, CA, USA. ¹⁶Department of Bioengineering, University of Illinois at Urbana-Champaign, Urbana, IL, USA. ¹⁷Department of Automation, Tsinghua University, Beijing, China. ¹⁸Cancer Center at Illinois, University of Illinois at Urbana-Champaign, Urbana, IL, USA. ¹⁹Departments of Civil and Environmental Engineering, Northwestern University, Evanston, IL, USA. ²⁰Wearifi, Evanston, IL, USA. ²¹Department of Neurological Surgery, Feinberg School of Medicine, Northwestern University, Chicago, IL, USA. ✉e-mail: jkchang@mywearifi.com;jrogers@northwestern.edu

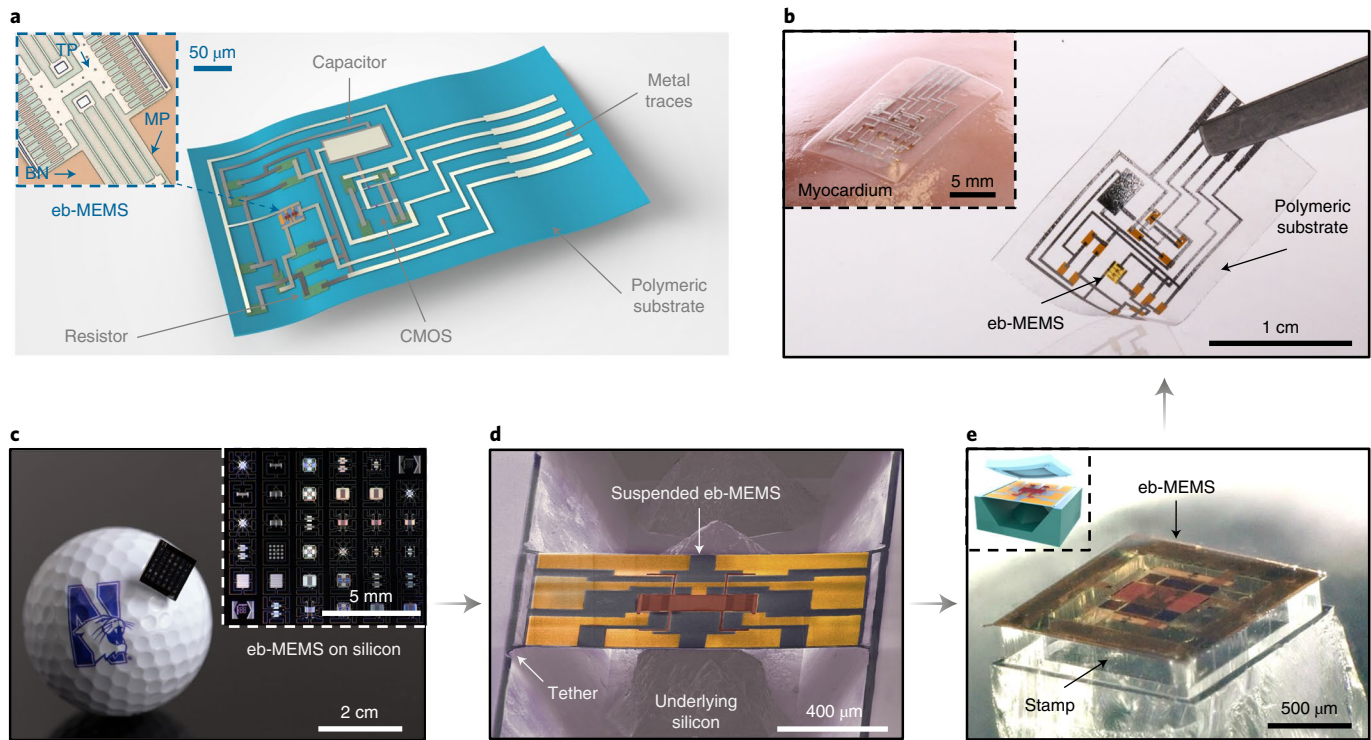


Fig. 1 | Eco-/bioresorbable flexible forms of eb-MEMS. **a**, Schematic illustration of a flexible eb-MEMS platform, highlighting the CMOS electronics, resistors, capacitors and the bioresorbable polymer substrate. The inset shows the eb-MEMS, which includes a top structural polysilicon layer as the moving/vibrating component (TP; thickness, 2 μm) with multiple combs (dimensions, 40 $\mu\text{m} \times 3 \mu\text{m} \times 2 \mu\text{m}$), an intermediate polysilicon layer as a stationary component (MP; thickness, 500 nm) and a bottom silicon nitride insulating layer (BN; thickness, 600 nm). **b**, Photograph of a flexible system. The inset shows an image illustrating integration onto the curved surface of the myocardium. **c**, Standard surface processing yields eb-MEMS structures on a silicon wafer. The inset shows a variety of eb-MEMS devices supported within a single die (1 cm \times 1 cm). **d**, Patterning and anisotropic etching procedures release these devices from the wafer to yield suspended layouts with four nitride tethers that connect the corners to the wafer. **e**, eb-MEMS on a stamp after retrieval from the source silicon wafer. The inset shows a schematic illustration of a stamp with a central recessed structure (dimensions, 1 mm \times 1 mm \times 180 μm) and four microtips (39 $\mu\text{m} \times 39 \mu\text{m} \times 28 \mu\text{m}$) at the corners to facilitate transfer printing.

reduce damage, confine mobile fragments and provide robust adhesion with adjacent tissues.

Eco-/bioresorbable forms of MEMS

A schematic illustration of an eb-MEMS (top-left inset) on a bioresorbable polymer substrate is shown in Fig. 1a. The device (dimensions, 1 mm \times 1 mm) includes a top layer of doped polysilicon as the moving/vibrating component (TP; thickness, 2 μm ; sheet resistance, $10 \Omega \text{sq}^{-1}$) with interdigitated combs (dimensions of cross-sectional area, 3 $\mu\text{m} \times 2 \mu\text{m}$), a middle layer of doped polysilicon as the stationary component (MP; thickness, 500 nm; sheet resistance, $28 \Omega \text{sq}^{-1}$) and a bottom insulating layer of silicon nitride (BN; thickness, 600 nm). A film of a bioresorbable polyanhydride-based polymer (PAP; thickness, 100 μm) serves as a flexible substrate. The complementary metal–oxide–semiconductor (CMOS) electronics, resistors and capacitor utilize a multilayer structure of SiO₂/Si/SiO₂/W/SiO₂/SiN_x (thickness, 1,000/100/700/400/700/600 nm; dimensions, 50 $\mu\text{m} \times 100 \mu\text{m}$), doped monocrystalline silicon micromembranes (Si MMs; thickness, 1,500 nm; sheet resistance, $40 \Omega \text{sq}^{-1}$) and a trilayer of Mo/SiO₂/W (thickness, 300/100/300 nm), respectively. The electrical connections employ two layers of tungsten and molybdenum (thickness, 300 nm each) with an interlayer dielectric of SiO₂ (thickness, 100 nm) to prevent crosstalk. The entire bioresorbable system is mechanically flexible (Fig. 1b and Supplementary Fig. 1) to enable ease of integration with soft, curved tissue surfaces, such as those encountered in biomedical applications. Figure 1b (top-left inset) exemplifies a device of this type mounted on the myocardium of a porcine model.

The fabrication processes and integration strategies, including the schemes in microfabrication, transfer printing and stencil patterning, are shown in Fig. 1c–e (Methods; Supplementary Notes 1 and 2 and Supplementary Tables 1 and 2 describe the details). Here lithographic processing yields collections of eb-MEMS on a source silicon substrate (Fig. 1c). Figure 1c (white inset) highlights the variety of eb-MEMS that can be formed on a single 1 cm \times 1 cm die. Examples include single-/dual-axis accelerometers, in-plane/out-of-plane linear/rotary electrostatic actuators/micromechanical resonators (μ -resonators), gyroscopes, biomorph/chevron electrothermal actuators, magnetic sensors, gear arrays and viscosity sensors (Supplementary Fig. 2). A sequence of patterning steps (Supplementary Fig. 3) and anisotropic etching procedures (Supplementary Fig. 4) selectively eliminate silicon from beneath the eb-MEMS to create suspended configurations with four silicon nitride tethers that connect to the surrounding wafer diagonally at each other (Fig. 1d). Gentle pressure applied to the devices with a soft elastomeric stamp (poly(dimethylsiloxane) (PDMS)) with a central recessed structure (dimensions, 1 mm \times 1 mm \times 180 μm) and microtips (39 $\mu\text{m} \times 39 \mu\text{m} \times 28 \mu\text{m}$) at its four corners (Fig. 1e (top-left inset), Supplementary Figs. 5–8 and Supplementary Note 3) fractures the tethers, such that the removal of the stamp retrieves a selected collection of eb-MEMS that are adhered by van der Waals interactions onto its surface. Figure 1e shows the stamp after this process, where contact only occurs at the microtip locations, thereby avoiding the potential for damage that might arise from direct contact between the stamp and fragile three-dimensional (3D) structures of the eb-MEMS. Transfer printing of the eb-MEMS

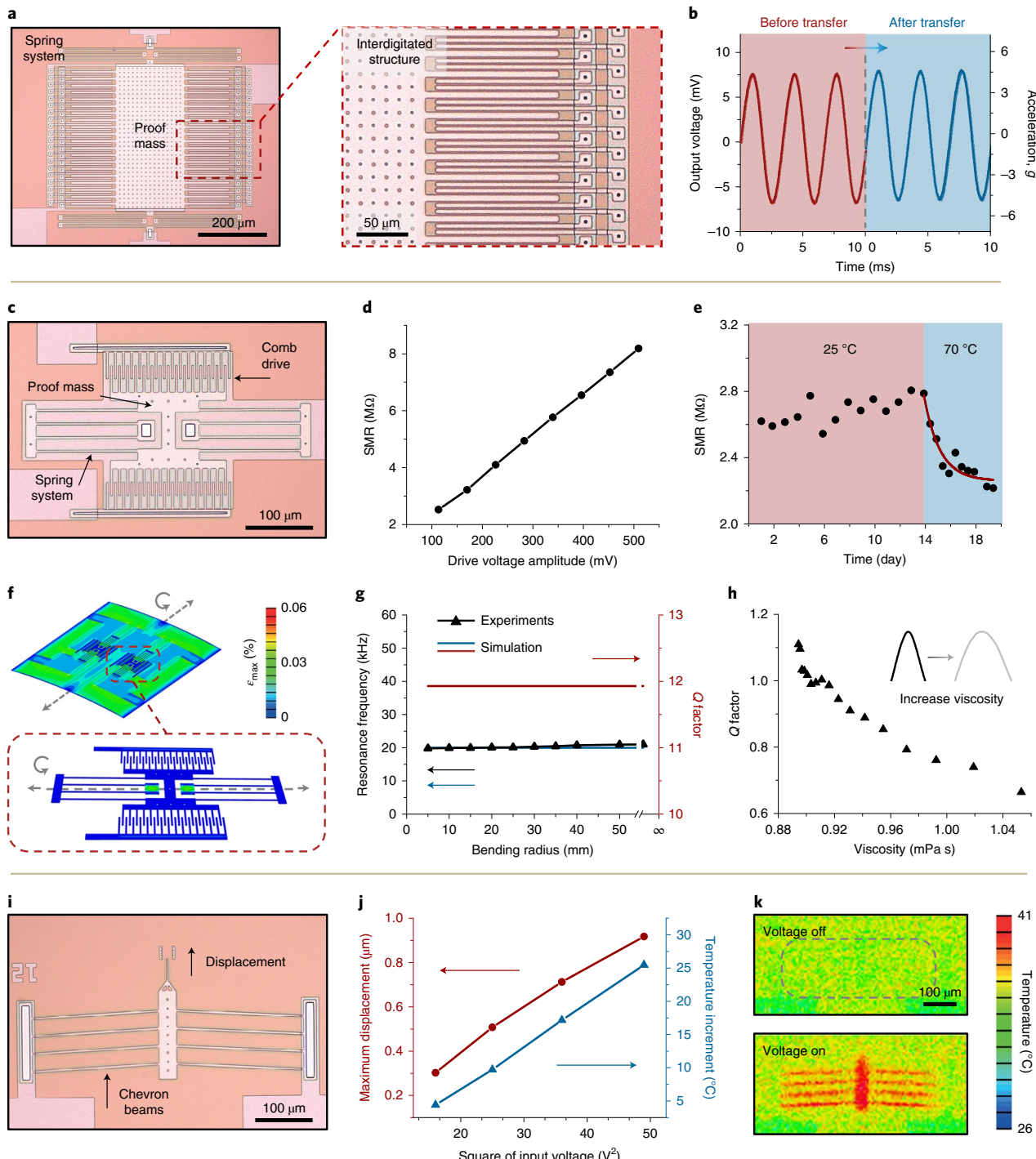


Fig. 2 | Representative classes of eb-MEMS. **a**, A bioresorbable differential single-axis accelerometer includes a suspended central rectangular film as the proof mass, suspended serpentine structures as the spring systems and suspended interdigitated electrodes for capacitance sensing. The inset shows the interdigitated structures comprising fingers on the bottom side that move with the proof mass along the direction of the body force and two stationary pairs of combs on the top side. **b**, Output voltage responses of devices on flexible polymeric substrates (cyan) and on the source wafer (red), in terms of the waveforms shapes, peak values (-7.5 mV) and frequency (300 Hz). **c**, A bioresorbable linear-type μ -resonator. Longitudinal comb-drive structures initiate vibrations of the proof mass with elastic restoring forces provided by the spring system. **d**, Linear dependence of the SMR on drive voltage. **e**, A μ -resonator exhibits stable performance after immersion in PBS (pH 7.4) at 25 °C for two weeks. Accelerated dissolution at 70 °C leads to a reduction in the SMR within the following six days. **f**, Maximum principal strain distributions across TP, MP and BN, at a radius of curvature of 5 mm. **g**, Performance of μ -resonators as they are bent to radii of curvature ranging from 5 mm to ∞ . Experimental resonance frequency (RF; marked black) of the μ -resonators changes only slightly with bending. The experimental results are consistent with the computed resonance frequency characteristics (marked cyan) and Q factors (marked red). **h**, Q-factor-based approach for viscosity measurement. Q factor for ethylene glycerol-water solutions with concentrations between 0 and 4%. Increasing the concentration of ethylene glycerol increases the viscosity (viscosity, 0.89–1.02 mPa s). **i**, An in-plane chevron electrothermal actuator. **j**, Maximum displacement and temperature increment at the chevron structure linearly depend on the square of the input voltage. **k**, Microradiometric thermal imaging of such a device for a representative input voltage (4 V).

and peripheral CMOS circuits onto a film of PAP (Supplementary Fig. 9), followed by the removal of sacrificial materials and stencil patterning for an associated set of capacitors and metal connections (Supplementary Fig. 10), completes the fabrication and integration process (Supplementary Note 4).

Representative classes of eb-MEMS

Electrocapacitive sensing, electrostatic actuation and electrothermal actuation represent the three main classes of MEMS technologies rendered in ecoresorbable and bioresorbable forms. Figure 2a shows a differential single-axis accelerometer. The TP layer includes a suspended central rectangular film (dimensions, $200\text{ }\mu\text{m} \times 420\text{ }\mu\text{m} \times 2\text{ }\mu\text{m}$) as the proof mass, a collection of suspended serpentine structures (cross-sectional area, $3\text{ }\mu\text{m} \times 2\text{ }\mu\text{m}$; length, 2 mm) as the spring systems (stiffness, $\sim 0.02\text{ N m}^{-1}$) and suspended interdigitated electrodes for capacitance sensing (Fig. 2a (red inset); dimensions of moveable fingers, $130\text{ }\mu\text{m} \times 6\text{ }\mu\text{m} \times 2\text{ }\mu\text{m}$ and quantity of 40; dimensions of fixed combs, $140\text{ }\mu\text{m} \times 4\text{ }\mu\text{m} \times 2\text{ }\mu\text{m}$, and quantity of 40 per pair). The voltage outputs of the accelerometer devices on bioresorbable PAP substrates (peak values, $\sim 7.5\text{ mV}$; Fig. 2b (cyan), Supplementary Fig. 11, Supplementary Note 5 and Supplementary Table 3) in response to a periodic sinusoidal vibration are consistent with those measured on source silicon wafers (Fig. 2b (red)) and with the theoretical values (Supplementary Fig. 12). Such consistency in the performance of eb-MEMS indicates that the device characteristics do not change after the complete set of processing steps outlined earlier.

Another example of an eb-MEMS device is the electrostatic actuator/ μ -resonator. Figure 2c presents a case of a linear-type μ -resonator (stiffness of the spring system, $\sim 7\text{ N m}^{-1}$) on a PAP film (thickness, $100\text{ }\mu\text{m}$), with a layer of molybdenum (thickness, 300 nm) as a bioresorbable electrical connection. Actuation follows from electrostatic forces that couple between two electrically conductive polysilicon combs (Fig. 2f (red inset); dimensions, $40\text{ }\mu\text{m} \times 3\text{ }\mu\text{m} \times 2\text{ }\mu\text{m}$; quantity, 15 per side). Stable performance of the actuator after immersion in a phosphate-buffered saline (PBS) solution ($\text{pH }7.4$) at various driving voltages is shown in Supplementary Fig. 13, and details of the encapsulation strategies and readout circuits are provided in Supplementary Table 3. The equivalent series motional resistance (SMR) as a function of the drive level represents an important performance characteristic^{32,33}. The expression $R_x = V_{\text{r.m.s.}}/i_x = -R_f/[V_{\text{output}}/V_{\text{r.m.s.}}]$ defines the SMR, where R_f is the large feedback resistor and $|V_{\text{output}}/V_{\text{r.m.s.}}|$ is the magnitude of the input-to-output voltage transfer function. The SMR exhibits a linear dependence on the drive amplitude (Fig. 2d), consistent with expectations based on studies of conventional MEMS resonators³².

Stable operation after immersion for a relevant period in biofluids and during bending is imperative for a device of this type, particularly for those applications requiring biointegration. The SMR at 80 mV remains $2.69 \pm 0.08\text{ M}\Omega$ after immersion in PBS ($\text{pH }7.4$) at 25°C for two weeks (Fig. 2e). Accelerated dissolution at 70°C leads to a reduction in SMR to $\sim 2.20\text{ M}\Omega$ in the following six days, which agrees well with simulation results (Supplementary Fig. 14). Computed results by 3D finite element analysis (FEA) for the distributions of maximum principal strains in the eb-MEMS, across the TP, MP and BN components, are shown in Fig. 2f (inset) and Supplementary Figs. 15 and 16, at a radius of curvature of 5 mm along two perpendicular axes, which is comparable to those of the myocardium in a rat model. The maximum strain, which occurs at the fixed-comb component in the TP layer, is less than 0.1%, well below the fracture strains of the constituent materials ($\sim 1.0\%$)³⁴. Experimental results (Fig. 2g (black)) demonstrate that the resonance frequency of the μ -resonator changes only slightly with bending, from 20.975 kHz on a flat surface (radius, ∞) to 20.230 kHz at a radius of 5 mm. Figure 2g shows that the device performance is

consistent with the computed resonance frequency characteristics (marked cyan) and quality (Q) factors (marked red).

In addition, the μ -resonators offer sensing capabilities that follow from dissipative processes associated with viscous and mass-loading effects of the surroundings. Studies of devices immersed in aqueous ethylene glycol solutions (concentration, 0–4%) demonstrate this functionality as changes in the Q factor. Increasing the concentration raises the viscosity (from 0.89 to 1.02 mPa s) but not the density (only from 0.997 to 1.002 g cm^{-3}). As the viscosity increases, the Q factor decreases (Fig. 2h and Supplementary Fig. 17) as an approach for using this parameter to determine the viscosity^{35,36}. Although the Q factor decreases to ~ 1 in an aqueous solution, the dependence on viscosity follows the equation $Q \propto 1/(\alpha\eta + \beta\sqrt{\eta} + \gamma)$ (η is the viscosity; α , β and γ are inherent coefficients). An attractive feature of this system is its ability to perform measurements on small volumes of liquid samples. Other μ -resonator designs include out-of-plane devices in isolated forms or arrays (Supplementary Fig. 18).

For electrothermal actuation, where the thermal expansion of strategic parts of a device results in large deflections, eco-/bioreversible forms of asymmetric (biomorph) and symmetric (chevron) designs are both demonstrated (Supplementary Fig. 2g,h). Optical and thermal characterization of a chevron-type example are shown in Fig. 2i and Supplementary Fig. 19. The data in Fig. 2j show that the maximum displacement and temperature increment linearly depend on the square of the input voltage (frequency, 1 Hz), with values that can reach several hundred nanometres. Microradiometric thermal imaging of such devices without and with an applied voltage (Fig. 2k) highlights the thermal distributions ($\Delta T_{4\text{V}} = 4.4 \pm 0.1^\circ\text{C}$; $\Delta T_{7\text{V}} = 25.5 \pm 0.2^\circ\text{C}$).

Eco-/bioreorption and biocompatibility of eb-MEMS

A defining characteristic of the eb-MEMS described here is that all the constituent materials resorb to eco-/biocompatible end products, in a controlled manner and within a relevant timeframe when exposed to biofluids or ground water. Studies of the resorption processes are performed at both the material level (Fig. 3a–c) and the device level (Fig. 3d). Critical constituent materials, namely, TP, MP and BN, react in aqueous environments via hydrolysis to yield silicic acid, hydrogen gas and ammonia ($\text{Si} + 4\text{H}_2\text{O} \rightarrow \text{Si(OH)}_4 + 2\text{H}_2$; $\text{Si}_3\text{N}_4 + 12\text{H}_2\text{O} \rightarrow 3\text{Si(OH)}_4 + 4\text{NH}_3$). Figure 3a–c present the kinetics of the accelerated dissolution of TP, MP and BN in PBS ($\text{pH }7.4$) at 70°C , evaluated as changes in the thicknesses of layers of each of these materials. The MP, TP and BN layers dissolve at rates of 31.0 ± 3.0 , 27.0 ± 2.0 and $1.7 \pm 0.1\text{ nm d}^{-1}$, respectively. The estimated degradation rates at 37°C are ~ 1.10 , 1.00 and 0.06 nm d^{-1} , respectively, according to Arrhenius scaling³⁷. The materials for electrical interconnection (that is, tungsten and molybdenum) oxidize in biofluids to yield a soluble acid ($2\text{W} + 2\text{H}_2\text{O} + 3\text{O}_2 \rightarrow 2\text{H}_2\text{WO}_4$; degradation rate, $\sim 150\text{ nm d}^{-1}$ in PBS ($\text{pH }7.4$) at 37°C ; $2\text{Mo} + 2\text{H}_2\text{O} + 3\text{O}_2 \rightarrow 2\text{H}_2\text{MoO}_4$, degradation rate, $\sim 20\text{ nm d}^{-1}$ in PBS ($\text{pH }7.4$) at 37°C)³⁸. Resorption of the substrate, that is, PAP, follows from chain scission processes associated with the hydrolytically labile anhydride bonds³⁹.

These chemical reactions proceed in parallel at the device level (Fig. 3d and Supplementary Fig. 20) as shown for an accelerometer collected at various stages of accelerated dissolution in PBS ($\text{pH }7.4$) at 70°C . The 3D mechanical structures persist from day 0 to day 5. On day 6, dissolution of the suspended proof mass leads to fracture of the TP film and corresponding generation of silicon fragments, such as those (thickness, $2\text{ }\mu\text{m}$; width, $3\text{--}6\text{ }\mu\text{m}$; length, $>200\text{ }\mu\text{m}$) from the combs and springs. The accelerometer fully disassembles and dissolves after day 20. During dissolution, the connection pads, namely, molybdenum, completely dissolve by hydrolysis. Packaging materials and related strategies provide solutions to confine these mobile fragments, as addressed in subsequent sections.

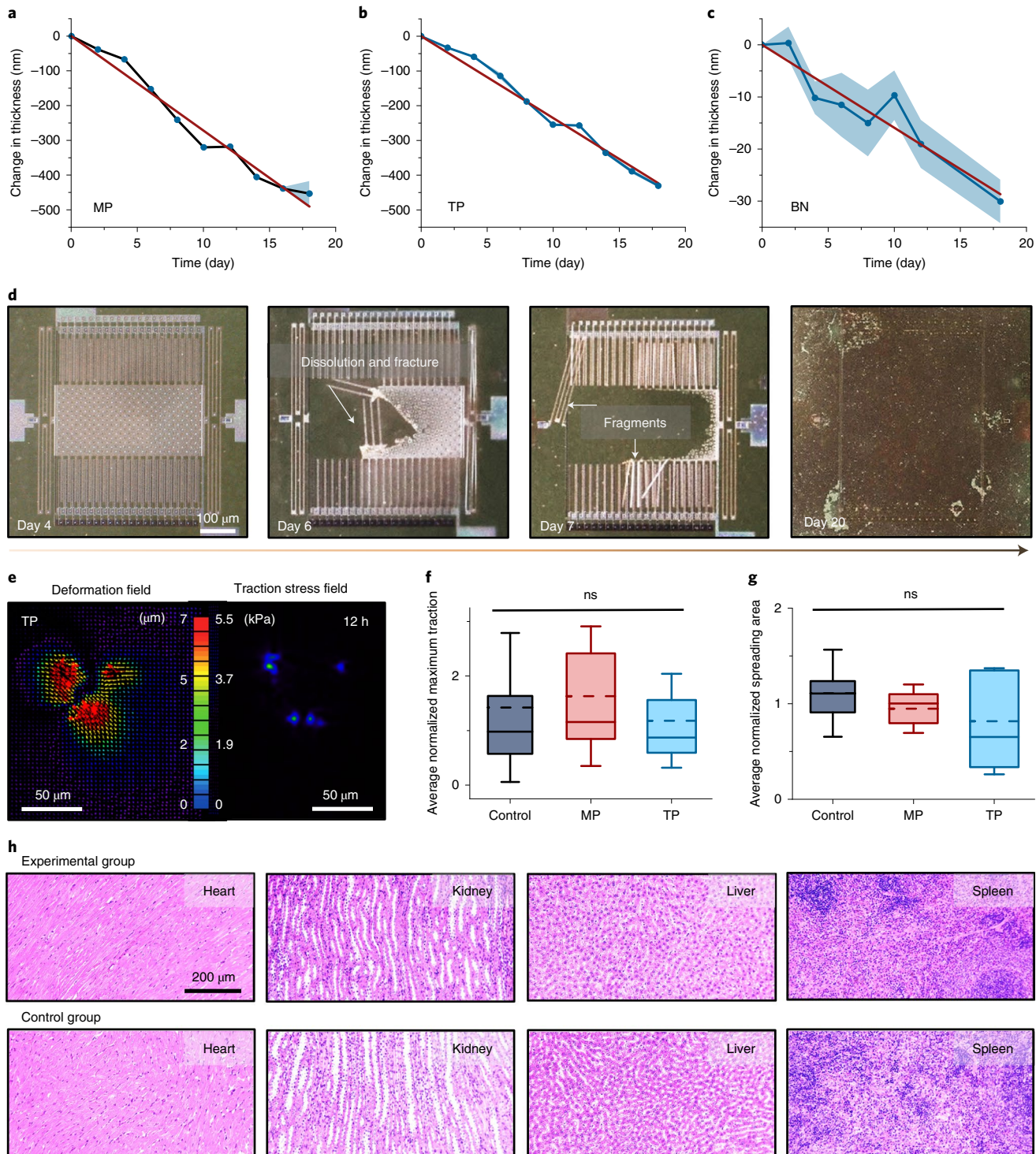


Fig. 3 | Eco-/biore sorption and biocompatibility of eb-MEMS. **a–c**, Accelerated dissolution kinetics of MP (**a**), TP (**b**) and BN (**c**) in PBS (pH 7.4) at 70 °C, evaluated as changes in the thickness, with linear dissolution rates of 31.0 ± 3.0 , 27.0 ± 2.0 and $1.7 \pm 0.1 \text{ nm d}^{-1}$. The shaded areas denote the standard deviation. **d**, Kinetics of dissolution of an accelerometer at various stages after immersion in PBS (pH 7.4) at 70 °C. **e**, Deformation field and traction stress map through cell-extracellular mechanotransduction analysis of a representative cell (CAF05) under culture media conditioned in the presence of TP extract (concentration, 1 mM) after 12 h. **f,g**, Quantitative analysis of average normalized maximum traction stress ($F(2,15) = 0.2150$, $P = 0.8090$) (**f**) and average normalized spreading area ($F(2,15) = 0.6520$, $P = 0.5351$) (**g**) for the cells exposed to MP-/TP-dissolved culture media after 10 h. The corresponding values for MP extracts are 1.6 ± 1.3 and 0.9 ± 0.3 and TP extracts are 1.2 ± 0.9 and 0.8 ± 0.6 , respectively; the results for the control samples are 1.4 ± 1.4 and 1.1 ± 0.5 , respectively. Whisker top, mean value + standard deviation; box top, 75% value; middle solid line, median value; middle dashed line, mean value; box bottom, 25% value; whisker bottom, mean value - standard deviation. **h**, H&E-stained sections of the representative vital organs (heart, kidneys, liver and spleen) from rats implanted with eb-MEMS devices, compared with controls. $n=3$ independent samples in **a–c**, **f** and **g**, and $n=3$ biologically independent animals in **h**. Values in **a–c**, **f** and **g** represent the mean \pm standard deviation. Statistical significance and P values are determined by one-way analysis of variance at a significance level of 0.05. ‘ns’ indicates no statistically significant differences.

Studies of biocompatibility, including detailed characterization based on mechanobiology⁴⁰, histology⁴¹ and haematology⁴², determine the safety of the eb-MEMS devices and associated end products on dissolution in biosystems. Mechanotransduction sourced from cellular traction, such as migration⁴³, cellular homoeostasis⁴⁴, differentiation^{45,46}, wound healing⁴⁷ and cancer metastasis^{48,49}, form the basis of detailed information on cytocompatibility. Accelerated dissolution of MP or TP in PBS (pH 7.4) at 85 °C, followed by dilution with additional culture media, yields media conditioned with MP or TP device extracts (concentration for each, 1 mM). Characterization with human colon fibroblasts (CAF05) in such culture media at 37 °C using traction force microscopy captures the aspects of cell–extracellular mechanotransduction. The results shown in Fig. 3e–g, Supplementary Figs. 21 and 22, Supplementary Note 6 and Supplementary Videos 1–3 indicate that the exposure of cells to device extracts does not change their traction or migration behaviours, including filopodial extrusion/retraction, movement and force homoeostasis. Representative deformation fields and traction stress maps of cells in the presence of MP and TP extracts appear in Fig. 3e and Supplementary Fig. 21. Supplementary Fig. 22a–c presents the average normalized (to the initial state) values of the maximum traction stresses, spreading areas and total traction forces associated with cells cultured in pure media and media with MP/TP extracts, from 5 to 12 h. The normalized traction parameters remain unchanged throughout the duration of exposure, consistent with negligible effects on metabolism and traction-related cellular functions such as maintaining cell shape, migrating within tissues and communicating with neighbouring cells. Changes appear after culturing for 10 h due to natural processes of cell division, indicating a negligible influence of MP and TP on cell physiology. Traction-associated parameters measured after 10 h appear in Fig. 3f,g and Supplementary Fig. 22d–f. The average normalized maximum traction stress, average normalized spreading area, average normalized traction stress, average normalized traction force and normalized total strain energy (to the initial state) for the cells exposed to culture media conditioned in the presence of MP extracts are 1.6 ± 1.3 , 0.9 ± 0.3 , 1.0 ± 0.5 , 1.3 ± 0.6 and 2.3 ± 1.8 , respectively. The corresponding values for TP extracts are 1.2 ± 0.9 , 0.8 ± 0.6 , 1.1 ± 0.2 , 0.9 ± 0.8 and 1.0 ± 1.6 , respectively. The results for the control samples (standard culture media) are 1.4 ± 1.4 , 1.1 ± 0.5 , 1.1 ± 0.6 , 1.2 ± 0.7 and 1.9 ± 1.7 , respectively. These findings confirm that the products of hydrolysis of the structural components of eb-MEMS have no measurable adverse effects on cell behaviours. Additional in vitro cytocompatibility studies of layers of MP and TP on silicon substrates reveal no observable decrease in cell viability (mouse fibroblasts) and proliferation after culturing for 24 h (Supplementary Fig. 23).

Histology and haematology studies in small animal models provide additional information on biocompatibility. After dorsal subcutaneous implantation for one month, haematoxylin and eosin (H&E)-stained sections of vital organs (heart, kidneys, liver, spleen, brain and dorsal skin) indicate no tissue damage and negligible appearance of immune cells related to the implantation and presence of eb-MEMS systems (Fig. 3h and Supplementary Fig. 24). Analysis of complete blood counts and blood chemistry (Supplementary Fig. 25) show normal levels of enzymes and electrolytes, including alanine aminotransferase, cholesterol and triglyceride, phosphorus and urea nitrogen, calcium, albumin, and total proteins, consistent with the absence of disorders in the liver, heart, kidneys, bone, nerve, as well as good overall health, respectively.

Encapsulation for biointegrated eb-MEMS

Encapsulation materials and associated deployment strategies are essential in the practical use of eb-MEMS. Figure 4a highlights several potential challenges in the context of applications that involve biointegration. First, fragile 3D structures can fracture or plastically

deform during interactions with biological tissues. Second, mobile fragments that form during the processes of dissolution can damage soft tissues (average animal cell size, 10–20 μm in diameter)⁵⁰ or occlude the flow of biofluids, particularly in small-diameter blood vessels (minimum feature sizes, 5–10 μm)⁵¹. Third, delamination from targeted mounting locations can lead to uncontrolled changes in position and orientation, with an adverse effect on intended modes of operation⁵². Strategies that address these challenges appear in Fig. 4b,c. Encapsulation methods, particularly for eb-MEMS that do not require direct contact (for example, accelerometers and gyroscopes) and that are susceptible to large deformations, are critically important in this context. For example, mixtures of bioresorbable natural wax materials (for example, candelilla wax and beeswax, 3:2 by weight ratio) can serve as robust, bioresorbable water barriers⁵³ (Fig. 4b) for accelerometers in sandwich architectures (thickness of each layer, 300 μm). The air space above the active region eliminates fracture or other forms of damage or degradation that could follow from contact with the wax. This encapsulation eliminates the potential for fracture or plastic deformation of the fragile 3D structures and prevents mobile fragments that form during the processes of dissolution. The power supply and associated interconnects are protected and isolated by the encapsulation materials to prevent direct contact with biological environments, thereby minimizing the risk of electrical leakage. Figure 4b (right) shows that the performance of a bioresorbable accelerometer remains unchanged during immersion in PBS (pH 7.4) at 37 °C for three days (output peak voltage, 4.2 ± 0.2 mV on day 0 and 3.8 ± 0.3 mV on day 3) under a periodic sinusoidal vibration (maximum acceleration, ~2.5 g; frequency, 100 Hz). On day 4, the voltage decreases to 0.8 ± 0.5 mV due to the permeation of water. Extended lifetimes can be achieved with the addition of inorganic bioresorbable barrier materials, such as monocrystalline silicon⁵³ and thermally grown SiO₂ (ref. ⁴²).

For devices that require contact with their surroundings (for example, μ-resonators for measurements of viscosity), the sensing elements (for example, silicon combs) can be encapsulated with a bioresorbable hydrogel adhesive matrix (HAM) (Fig. 4c). The HAM encapsulation and associated strategies enable the safe and effective use of contacting-type eb-MEMS in realistic scenarios, outside of the realm of any previously reported technology. A polylactide acid (PLA) capping structure (2 mm × 2 mm × 200 μm) with four holes (diameter, 600 μm) placed above the device (1.2 mm × 1.2 mm × 3 μm) eliminates direct contact between the eb-MEMS and HAM in a manner that retains direct access to biofluids. The HAM used here consists of covalently cross-linked bifunctional polyethylene glycol-polylactide-diacylate (PEG-LA-DA) macromers and ionically crosslinked sodium alginate (Supplementary Fig. 26). This matrix can provide robust adhesion to biological tissue surfaces to anchor the eb-MEMS for days or weeks, support diffusive access of proteins or molecules to the eb-MEMS for sensing, and confine device fragments that arise from fracture or partial disintegration due to dissolution.

Demonstrations of schemes that address these three challenges appear in Fig. 4d–f. As illustrated in Fig. 4d, primary amine groups on the chitosan backbone of the primer covalently bond with carboxylic acid groups on the tissue surfaces and alginate network in HAM to enable robust bonding, enhanced by physical chain entanglement. Strong adhesion occurs for biological tissues, with a representative example of skin shown in Fig. 4d, right (~ 300 J m⁻²). The HAM allows diffusive transport of proteins and other biomolecules, as illustrated using bovine serum albumin (BSA). Cross-sectional views obtained through confocal fluorescence microscopy reveal the dynamic diffusion processes inside the HAM at 37 °C (Supplementary Fig. 27). Ultraviolet-visible (UV-vis) spectroscopic results determine the concentration of BSA on both sides of a reservoir separated into two regions by a layer of HAM (diameter, 3 cm; thickness, 400 μm) at 37 °C (Fig. 4e and Supplementary Fig. 28).

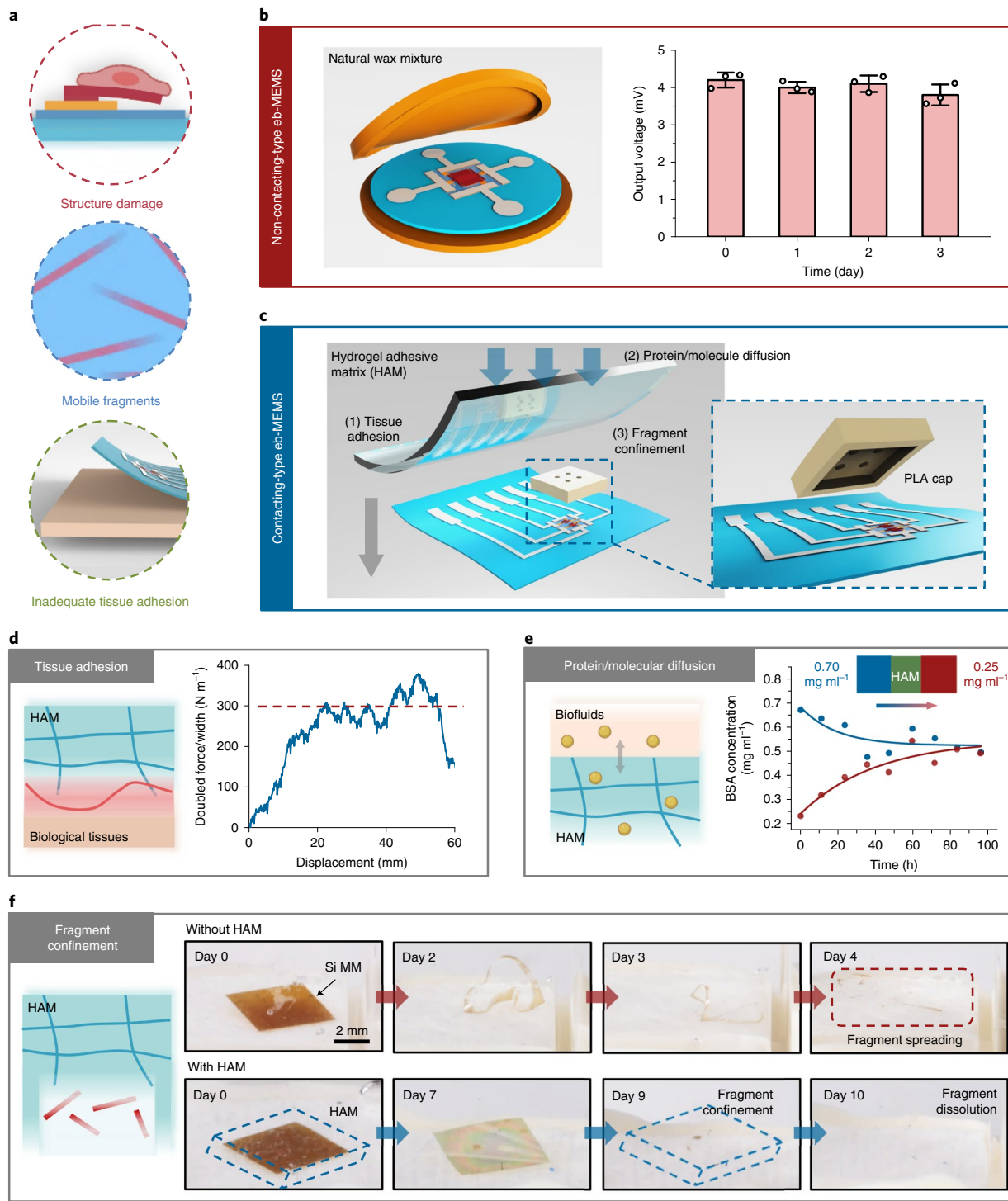


Fig. 4 | Encapsulation of eb-MEMS for eco-/biointegration. **a**, Potential challenges for eco-/biointegration include damage to the device, formation of mobile fragments and loss of adhesion to the tissue. **b**, Scheme that uses wax encapsulation with a non-contacting-type eb-MEMS (for example, accelerometer) in a sandwich architecture (left side; layer thicknesses, 300 μm) and performance data after immersion in PBS (pH 7.4) at 37 °C (right side; acceleration, ~2.5 g; frequency, 100 Hz). **c**, A bioresorbable HAM serves as the encapsulating material for a contacting-type eb-MEMS to provide robust adhesion to biological tissue surfaces for days to weeks, diffusive access of proteins or other biomolecules through the hydrogel matrix, and confinement for device fragments. **d**, Adequate tissue adhesion. Schematic illustration of the mechanisms for bonding to biological tissues (left). The primary amine groups on the chitosan backbone in the primer layers covalently bond with carboxylic acid groups on the tissue surfaces and alginate network in the hydrogel, with further enhanced bonding by physical chain entanglement. Plot of the doubled peeling force per width of the HAM versus displacement for HAM-tissue bonding (right). The data determine the adhesion energy (~300 J m^{-2}). **e**, Access to protein/molecular diffusion. Schematic illustration of diffusive access provided by the HAM (left). Diffusion of BSA through a layer of HAM at 37 °C, with a measured diffusivity of $3 \times 10^{-11} \text{ m}^2 \text{s}^{-1}$ (right). **f**, Confinement of mobile fragments. Utilization of a HAM to confine fragments produced from the eb-MEMS (left). Characterization of mobile fragments that form from the accelerated dissolution of Si MMs (4 mm \times 4 mm \times 1.5 μm) without (top row) and with (bottom row) the HAM layer (right). $n=3$ independent samples in **b**. The values in **b** represent the mean \pm standard deviation.

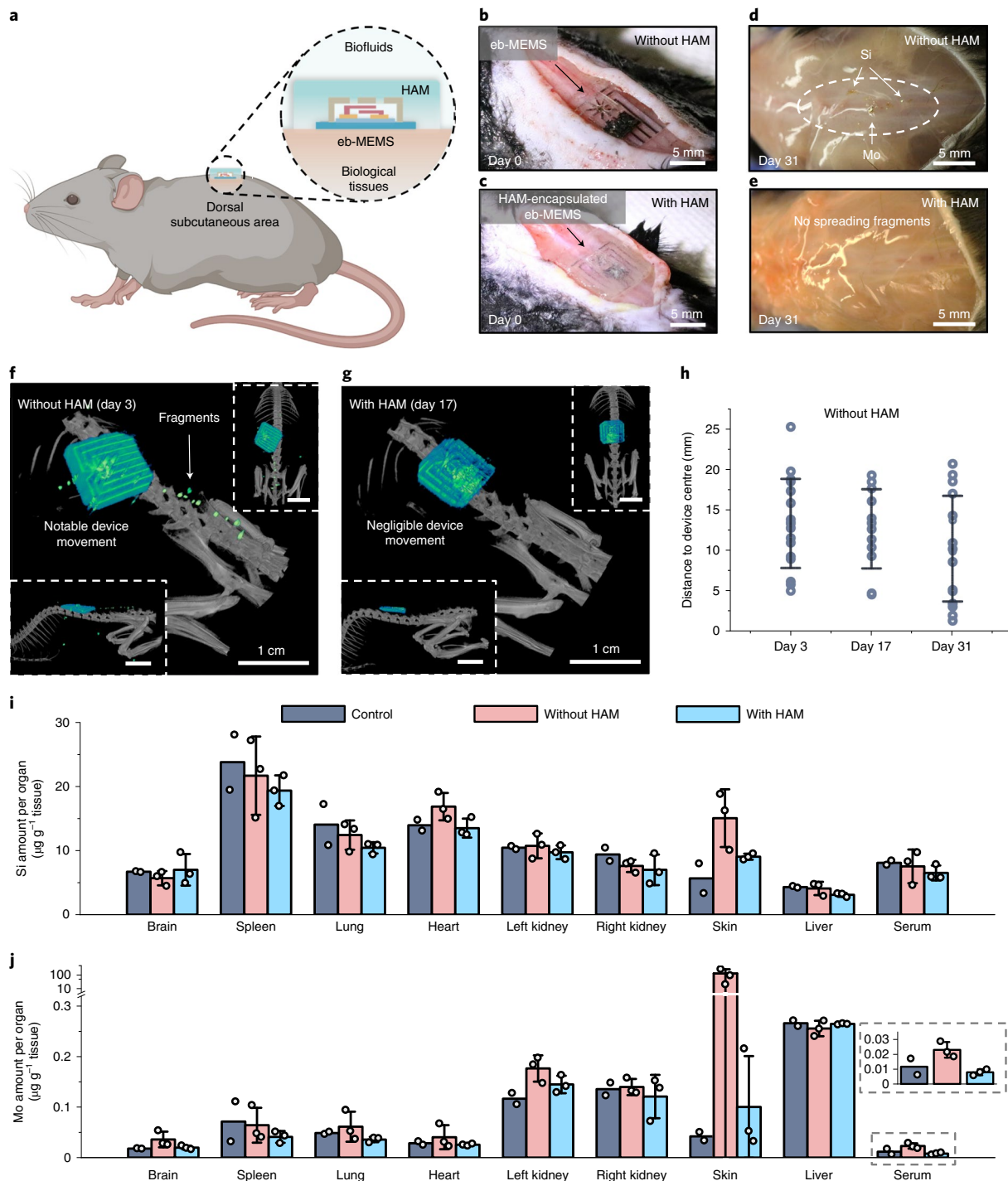


Fig. 5 | In vivo evaluations of an HAM-encapsulated eb-MEMS in a small animal model. **a**, Schematic of the implantation of eb-MEMS μ -resonators on dorsal subcutaneous tissues. **b,c**, Photographs of the eb-MEMS without (**b**) and with (**c**) the HAM layer. Adding additional fragments (Mo; used for eb-MEMS; $100\text{ }\mu\text{m}\times 100\text{ }\mu\text{m}\times 5\text{ }\mu\text{m}$; quantity, ~ 10) inside the HAM layer, along with the device itself, facilitates the observation of distribution in the animal model. **d,e**, Exposure of the dorsal subcutaneous tissues after euthanasia of the animals at day 31 post-surgery reveals that the fragments spread around the dorsal subcutaneous tissues without the HAM (**d**). By contrast, the HAM confines the fragments, thereby preventing their spreading into surrounding tissues (**e**). **f,g**, Positions of eb-MEMS and associated fragments without the HAM layer along the diagonal (main), sagittal (bottom-left) and coronal (top-right) directions at day 3 post-surgery. The device undergoes notable movement, and the fragments are spread across the surrounding tissues. **g**, Positions of eb-MEMS and associated fragments with the HAM layer at day 17 post-surgery. The device remains in the original location, and all the fragments remain underneath the HAM throughout the study, to within experimental uncertainties. **h**, Statistical analysis of the displacements of the fragments (original position, device centre) without the HAM are 13 ± 6 , 13 ± 5 and 10 ± 6 mm, respectively, at day 3, 17 and 31 post-surgery, respectively. **i,j**, Concentrations of silicon (Si) and molybdenum (Mo) in vital organ tissues from the analysis of explants harvested on day 31 post-surgery. The concentrations of elements in the group with the HAM-encapsulated eb-MEMS show similar distributions to those in the control group without implantation. By contrast, for eb-MEMS without the HAM, both elements present at higher concentrations compared with those with the HAM in most organ tissues. $n=2$ biologically independent animals for the control group and $n=3$ biologically independent animals without and with the HAM in **h–j**. The values in **h–j** represent the mean \pm standard deviation.

Initial concentrations (top side, 0.70 mg ml^{-1} in PBS; bottom side, 0.25 mg ml^{-1}) equilibrate to values of 0.50 mg ml^{-1} . Quantitative analysis defines the diffusivity of BSA in the HAM as $3 \times 10^{-11} \text{ m}^2 \text{s}^{-1}$ (Supplementary Note 7), comparable to that of other hydrogels^{54,55}. As mentioned previously, the HAM also confines fragments that may release from the device (Fig. 4f and Supplementary Fig. 29) for the case of a uniform layer of silicon ($4 \text{ mm} \times 4 \text{ mm} \times 1.5 \mu\text{m}$). For accelerated dissolution studies without the HAM in PBS (pH 7.4) at 70°C , the thickness of the silicon decreases through the first day and then begins to buckle on day 2. Many fragments appear on day 4, spread across the chamber, followed by full dissolution on day 5. With HAM encapsulation, the silicon remains in its initial position throughout the process, with slightly reduced dissolution kinetics under the hydrogel encapsulation. Specifically, the thickness of silicon decreases from day 0 to day 7 and then breaks into several fragments, which are confined by the HAM. The resulting fragments disappear by day 10.

Animal model evaluations

Additional animal model evaluations show that the HAM can anchor the device and confine mobile fragments for several weeks (Fig. 5a). Figure 5b,c and Supplementary Fig. 30 present the optical images of eb-MEMS μ -resonators implanted on dorsal subcutaneous tissues without and with an HAM layer. Adding separately fabricated molybdenum pieces associated with the eb-MEMS (dimensions, $100 \mu\text{m} \times 100 \mu\text{m} \times 5 \mu\text{m}$; quantity, ~10), along with the device itself, facilitates the observation of the distribution of fragments in the animal model. Exposure of the dorsal subcutaneous tissues after 31 days post-surgery reveals the positions of fragments in both cases (Fig. 5d,e). Without the HAM, the fragments spread across the dorsal subcutaneous tissues; by contrast, the presence of the HAM confines the fragments and prevents such spread.

Microcomputed tomography (microCT) images along the diagonal (main), sagittal (bottom-left) and coronal (top-right) directions across day 3 and 17 (Fig. 5f,g, Supplementary Fig. 31 and Supplementary Note 8) post-surgery quantifies the positional stability. The eb-MEMS without the HAM exhibits notable movement, and the fragments spread around the surrounding tissues after only 3 days post-surgery (Fig. 5f). By contrast, with the HAM, even after 17 days post-surgery, the devices and associated fragments remain in their original locations throughout the study (Fig. 5g). A statistical analysis (Fig. 5h) indicates that the average displacements of the fragments (original position, device centre) without the HAM encapsulation are $13 \pm 6 \text{ mm}$, with the maximum displacement of up to 25 mm . The corresponding values on day 17 and day 31 post-surgery are 13 ± 5 and $10 \pm 6 \text{ mm}$, respectively (animal body length, $75\text{--}100 \text{ mm}$)⁵⁶.

Studies of elemental biodistribution (silicon from eb-MEMS, molybdenum from eb-MEMS and additional pieces) without and with the HAM layer throughout various organ tissues in mouse models reveal additional features of this system. Figure 5i,j presents the concentrations of silicon and molybdenum in the brain, spleen, lung, heart, kidneys, skin, liver and serum explanted 31 days post-surgery, measured by inductively coupled plasma optical emission spectrometry (ICP-OES) and inductively coupled plasma mass spectrometry (ICP-MS). Without the HAM, silicon and molybdenum accumulate in the skin, with elevated concentrations in some other organs. These results are likely due to the broader distribution and faster dissolution of these elements without the HAM encapsulation. By contrast, the measured concentrations of critical elements (that is, silicon and molybdenum) in the group of animals with the HAM-encapsulated eb-MEMS exhibit much lower values, at levels closer to those in the control group without implants. The results demonstrate the ability of the HAM encapsulation to confine mobile fragments *in vivo*.

Conclusions

We have introduced MEMS devices that are fully ecoresorbable or bioresorbable, as well as associated encapsulation and deployment strategies for their use as biomedical implants. All the major classes of MEMS devices—electrocatalytic sensors, electrostatic actuators and electrothermal actuators—can be realized using these approaches. Our processing schemes enable transfer printing of multilayer 3D suspended and movable structures with bioresorbable characteristics at high levels of integration. These materials, fabrication and encapsulation strategies enabled such MEMS devices to be combined with appropriate substrates, interconnects, associated components (via transfer printing and stencil patterning) and encapsulation structures.

Bioresorption and mechanical flexibility are critical features for various possible future applications of MEMS devices, including those that require temporary operation in complex biological and environmental conditions. Resorption eliminates the need for extractive surgery for implantable medical devices and minimizes solid electronic waste from consumer gadgetry. Bioresorbable natural waxes and tissue-like HAM layers can be used as encapsulating materials for non-contacting- and contacting-type eb-MEMS, respectively; together with associated insertion strategies, they have been shown to avoid damage, confine mobile fragments and provide robust adhesion with adjacent tissues in both *in vitro* and *in vivo* studies. Our eb-MEMS devices could be combined with readout circuitry made with previously reported biodegradable silicon-based CMOS devices and integrated circuit technology¹⁶, providing the starting point for the development of highly integrated eb-MEMS/CMOS platforms.

Methods

Design and fabrication of eb-MEMS. Design and preprocessing. Designs for the eb-MEMS used the CoventorMP platform (MEMS+ and CoventorWare; Coventor) for parametric concept exploration, layout optimization and system-level circuit modelling. Fabrication of eb-MEMS on monocrystalline silicon wafers (surface orientation, (100) ; thickness, $675 \mu\text{m}$) followed a trilayer polysilicon surface micromachining process (PolyMUMPs; MEMSCAP), including (1) a dielectric bottom layer of silicon nitride (BN; thickness, 600 nm ; residual stress, $+89 \text{ MPa}$ (T)); (2) a conducting middle layer of polysilicon (MP; thickness, 500 nm ; residual stress, -29 MPa (C)); (3) a top moving/vibrating layer of polysilicon (TP; thickness, $2 \mu\text{m}$; residual stress, -4 MPa (C)); and (4) a sacrificial overcoat of phosphosilicate glass (thickness, $2.5 \mu\text{m}$). Spin casting at $3,000 \text{ rpm}$ for 30 s , followed by baking at 110°C for 70 s , formed a buffer layer of the photoresist (AZ 5214; MicroChemicals) above the eb-MEMS devices to prevent damage before processing for release and transfer printing.

Processing for tethered eb-MEMS suspended above silicon substrates. The procedures began with removal of the protective layer of photoresist by soaking in acetone for 5 min , followed by rinsing with isopropyl alcohol (IPA) and deionized (DI) water. A uniform layer of silicon dioxide (thickness, 500 nm) deposited by plasma-enhanced chemical vapour deposition (SPTS Technologies) fully embedded the structural polysilicon to serve as the material for the patterning barriers. Spin casting at $6,000 \text{ rpm}$ for 30 s , followed by baking at 110°C for 90 s , formed a layer of photoresist (AZ 4620; MicroChemicals) on top. Photolithographic exposure using a maskless aligner (MLA150; Heidelberg Instruments) at 800 mJ cm^{-2} , followed by immersion in a photoresist developer (AZ 400 K 1:2; MicroChemicals) for 30 s , exposed a trench area surrounding each eb-MEMS. Soaking in buffered oxide etchant (BOE; volume ratio of 40% ammonium fluoride (NH_4F) in water to 49% HF of 6:1; Sigma-Aldrich) for 15 min removed the sacrificial oxide from the exposed areas. Depositing a passivation layer of silicon nitride (thickness, $1 \mu\text{m}$; low-pressure chemical vapour deposition; Tystar) covered the sacrificial oxide on the eb-MEMS. Photolithographic patterning using the aforementioned recipe followed by reactive ion etching (RIE-10NR; recipe, $10 \text{ s.c.c.m. CHF}_3$; 1 s.c.c.m. O_2 ; 2 Pa pressure; 175 W RF; duration, $1,500 \text{ s}$; Samco) defined nitride tethers and exposed the underlying silicon near these tethers. The anisotropic undercut etching of silicon involved the complete immersion of such devices in a static solution of tetramethylammonium hydroxide (concentration, 25% ; Sigma-Aldrich) at 85°C for 18 h . The nitride tethers held the eb-MEMS in their lithographically defined locations after complete undercut to yield devices in suspended configurations in solution. Soaking in DI water (duration, 10 min) and HF (concentration, 49% ; duration, 10 min) in sequence, followed by critical point drying (Automegasamdry-915B; Tousimis), completed the process.

Processing of stamps for transfer printing. Fabrication of the structured stamps began with depositing a layer of silicon dioxide (thickness, 50 nm; plasma-enhanced chemical vapour deposition) on a silicon wafer (surface orientation, (100); thickness, 525 µm). Photolithography (AZ 4620; 3,000 rpm for 30 s), using a maskless aligner (MLA150) at 800 mJ cm⁻² followed by immersion in a photoresist developer (AZ 400K 1:2) for 60 s, and wet etching with BOE (6:1) for 30 exposed square patterns of underlying silicon (39 µm × 39 µm) designed to produce the microtip structures for the stamps. Following a step of photoresist stripping in acetone, anisotropic etching of the exposed silicon using a solution of potassium hydroxide (KOH; concentration, 18%; Sigma-Aldrich) at 70 °C for 45 min formed pyramidal recessed features with sidewalls at a 54.7° angle with the surface. After removing the deposited oxide by immersion in BOE (6:1) for 1 min, spin casting at 1,000 rpm for 60 s, followed by baking at 65 °C for 7 min and 95 °C for 45 min, formed a thick layer of SU-8 2050 photoresist (thickness, ~180 µm; MicroChemicals). Photolithographic exposure using a mask aligner (MA/BA6; SUSS MicroTec) for 540 mJ cm⁻², followed by post-exposure baking at 95 °C for 15 min and immersing in SU-8 developer (MicroChemicals) for 1 h, defined hollow square patterns (outside dimensions, 1.2 mm × 1.2 mm; inside dimensions, 1.0 mm × 1.0 mm). This process yielded pyramidal features at the four corners of each of the square patterns. Hydrophobic treatment of the processed wafer involved immersion in trichloro(octadecyl)silane (0.2 vol% in hexane; Sigma-Aldrich) for 10 min followed by rinsing with IPA and DI water. Curing a liquid precursor to PDMS (part A:part B = 10:1; SYLGARD 184; Dow Corning) against this SU-8/Si mould at 60 °C for 10 h yielded stamps with recessed features at the centres and microtips at the four corners.

Transfer printing. Transfer printing involved the retrieval of suspended eb-MEMS from the source wafer to the surface of a stamp, followed by the delivery of eb-MEMS from the stamp to a bioresorbable polymer substrate. Retrieval began with aligning the stamp to eb-MEMS with a manual mask aligner (MJB4; SUSS MicroTec) in the top-side alignment mode. Slowly lowering the stamp towards the substrate established initial contact to the suspended eb-MEMS device. Continued lowering led to the collapse of the microtips, followed by full collapse around the periphery of the stamp. Further lowering led to the breakage of the tethers. Retracting the stamp completed the retrieval process. A uniform layer of PAP served as the receiver substrate. Crosslinking a mixture of 4-pentenoic anhydride (8.7 wt%), 1,3,5-triallyl-1,3,5-triazine-2,4,6(1H,3H,5H)-trione (49.2 wt%), 1,4-butanedithiol (41.9 wt%) and 2-hydroxy-4'-(2-hydroxyethoxy)-2-methylpropiophenone (photoinitiator; 0.2 wt%) on a hydrophobic Si wafer, followed by ultraviolet (UV) exposure (wavelength, 365 nm; density, 590 µW cm⁻²) for 3 min, yielded a partially cured PAP film (thickness, 100 µm) with a tacky surface. Transferring the eb-MEMS from the stamp to the PAP, followed by exposure to UV light (wavelength, 365 nm; density, 590 µW cm⁻²) for another 10 min and baking at 150 °C for 3 h to fully cure the PAP film completed the transfer printing process.

Processing for stiction-free release of the eb-MEMS. Reactive ion etching (RIE-10NR; recipe, 10 s.c.c.m. ClF₃; 1 s.c.c.m. O₂; 2 Pa pressure; 175 W RF; duration, 1,500 s) removed the silicon nitride passivation layer of the printed eb-MEMS device. Soaking in a bath of HF (concentration, 49%) for 5 min to remove the phosphosilicate glass layer, followed by soaking in DI water for 30 min, soaking in IPA for 1 h and baking at 120 °C for 20 min, enabled the stiction-free release of the microscale structure of eb-MEMS. Depositing a layer of tungsten or molybdenum (thickness, 300 nm) by sputter deposition (AJA International) through a stainless-steel stencil mask (thickness, 50 µm; patterned by laser cutting; McMaster-Carr) defined the connection pads. The fabrication and transfer processes for CMOS (50 µm × 100 µm) and other electronic components followed the methods described previously^{57,58}. A layer of SiO₂ (thickness, 20 nm) could be formed using an atomic layer deposition system (GEMStar XT-P, Arradiance) for improved protection.

Evaluation of dissolution kinetics. Material-level evaluations. Spin coating of the photoresist (AZ nLOF 2035; MicroChemicals) at 4,000 rpm for 40 s, followed by baking at 110 °C for 60 s, formed a mask layer on a die (1 cm × 1 cm) cut from a MEMS wafer. Photolithographic exposure using a mask aligner (MA/BA6; SUSS MicroTec) for 90 mJ cm⁻², followed by immersion in a photoresist developer (AZ 300 MF; MicroChemicals) for 30 s, exposed square patterns (100 µm × 100 µm) of the photoresist in the TP, MP and BN areas. Electron-beam evaporation of a bilayer of Cr/Au (thickness, 10/100 nm), followed by a lift-off process in acetone formed exposed square patterns (100 µm × 100 µm) in the corresponding TP, MP and BN areas. Immersing the MEMS wafer die in a polytetrafluoroethylene (PTFE) bottle filled with PBS (pH 7.4; volume, ~20 ml) at 70 °C resulted in the accelerated dissolution of the exposed TP, MP and BN. The replacement of PBS (pH 7.4) occurred every other day. Imaging with a 3D laser confocal microscope (OLS5000; Olympus) defined changes in the heights of the exposed surfaces compared with the edges of the deposited inert metals (Cr/Au).

System-level evaluations. Optical images captured with a digital microscope (VHX-6000 series; Keyence) characterized the dissolution behaviours of the

combs, springs and completed devices. Immersion of eb-MEMS on the PAP substrate in a PTFE bottle filled with PBS (pH 7.4; volume, ~20 ml) enabled accelerated dissolution. Replacement of PBS (pH 7.4) occurred every other day.

Mechanical simulations. Designs and FEA for the transfer printing process.

Three-dimensional FEA simulations were used to evaluate the stresses in the nitride tethers during the transfer process. Pressure delivered to the stamp fractured the tethers to allow the retrieval of eb-MEMS. Further, 3D solid elements were used for the stamp, and shell elements were used for devices with tethers in commercial FEA software (Abaqus; Simulia). After a total of 50 µm displacement was applied on top of the stamp, the predicted stresses exceeded 2 GPa, which was much larger than the typical tensile strength for the nitride (~500 MPa), consistent with experiments.

FEA for eb-MEMS accelerometers. Three-dimensional FEA analysis in commercial FEA software (COMSOL Multiphysics; COMSOL) predicted the output voltage of the accelerometer in acceleration. The structure-electric coupling module with the steady-state solution in COMSOL Multiphysics predicted the capacitance of the accelerometers in acceleration. The acceleration effect (*a*) was modelled by inertial force (*pag*; *g*, gravitational constant) per unit volume applied as the body force on the accelerometer. The capacitance was finally converted to the output voltage based on the experimental setup.

FEA for eb-MEMS μ-resonators under bending. Three-dimensional FEA analysis with 3D solid elements in commercial FEA software (Abaqus; Simulia) predicted the bending-induced strain, resonant frequency and Q factor of the eb-MEMS in an air environment. The elastics module of Abaqus predicted the deformed shape, strain and stress distribution in eb-MEMS under bending, and transferred them to the steady-state dynamics module to predict the relationship of vibration amplitude (*A*) versus frequency (*f*). Resonant frequency and Q factor were then calculated based on the *A* versus *f* curve. To excite the vibration, the displacement boundary conditions were applied in the *y* direction in the region where the eb-MEMS was attached to the substrate. A stiffness-proportional damping factor of $\beta = 3 \times 10^{-7}$ was introduced to model the dissipation of the system. The material properties were Young's modulus *E* = 180 GPa, Poisson's ratio ν = 0.22 and mass density ρ = 2.23 g cm⁻³.

FEA for eb-MEMS μ-resonators in liquid environment. Three-dimensional FEA analysis in commercial FEA software (COMSOL Multiphysics, COMSOL) predicted the Q factor of the μ-resonators in the liquid environment of an ethylene glycol-water mixture. The structure-acoustic coupling module with a steady-state solution in COMSOL Multiphysics predicted the relationship of vibration amplitude (*A*) versus frequency (*f*) to obtain the Q factor. The μ-resonators and surrounding liquid were modelled by 3D solid element and 3D acoustic element, respectively. The density of the ethylene glycol-water mixture remained $\rho_{\text{liquid}} = 1.00 \text{ g cm}^{-3}$ and a parameter study was performed for viscosity μ_{liquid} in the range of 0.80–1.20 mPa s.

Evaluation of bioresorbable accelerometers. Electrical characterization.

Interfacing a bioresorbable accelerometer with a capacitive readout circuit evaluation board (Irvine Sensors) enabled signal capture with an oscilloscope (SIGLENT Technologies). A commercial accelerometer (Kistler) served as a reference device to calibrate the measurements. Out-of-plane vibrations resulted from a shaker (3B Scientific) powered by a function generator (3B Scientific) to achieve periodic sinusoidal programmable accelerations. Mounting the bioresorbable accelerometer and commercial reference device on the shaker with their sensing axis along the vibration axis (*z* axis), by aligning the edges of the devices to the edges of the vertical square sample holder, ensured the alignment of the input axis for both devices.

Evaluation of bioresorbable in-plane/out-of-plane electrostatic actuators.

Electrical characterization. Applying a driving a.c. voltage ($V_{\text{r.m.s.}}$) from a waveform function generator (SIGLENT Technologies) and a high-voltage amplifier (Falco Systems) to the fixed-comb electrode, along with a d.c. voltage ($V_{\text{d.c.}}$; Sky Top Power) to the moving mass, launched in-plane vibrations of the bioresorbable electrostatic actuators/μ-resonators. Pick-up current from the sensing capacitor, preamplified by a transimpedance amplifier (DigiKey Electronics) with 1 MΩ gain, defined the converted readout voltage shown in a spectrum analyser (Rigol Technologies). Characterizing the device performance in a vacuum environment suppressed the effect of feedthrough currents³². For the long-term immersion test, each measurement starts after the drying of the devices using a critical point dryer (Tousimis).

Optical characterization. Observations of the vibration of the electrostatic actuators utilized a microscope scanning vibrometer (MSV; 400 series; Polytec). Applying $V_{\text{r.m.s.}}$ from a waveform function generator (SIGLENT Technologies) and a high-voltage amplifier (Falco Systems) to the two-comb electrodes activated in-plane vibrations. Slightly tilting the devices (tilt angle, ~20°) facilitated measurements of these motions with the MSV. A custom software routine created

using LabVIEW (National Instruments) yielded displacements associated with the vibrations. Mounting the electrostatic actuator onto 3D-printed plastic curved moulds (bending radius, 5–40 mm) enabled optical measurements under different bending radii. The characterization for out-of-plane devices utilized the same MSV and LabVIEW software mentioned above.

Evaluation of bioresorbable chevron in-plane electrothermal actuators.

A microradiometric thermal imaging microscope (Optotherm) captured the temperature distribution over the surfaces of the actuators. Images from a digital microscope (VHX-6000 series; Keyence) captured the in-plane displacements. An open-source software package, ImageJ, facilitated the measurements of displacement^{59,60}.

Wax packaging for non-contacting-type eb-MEMS. Fabrication processing.

A mixture of natural wax materials served as the encapsulation for non-contacting-type eb-MEMS. The fabrication process began with the melting of candelilla wax and beeswax in a weight ratio of 3:2 at 85 °C. Drop casting the melted wax mixture into a PDMS mould with a trench (dimensions, 2 cm × 2 cm × 300 µm) and cooling to room temperature yielded uniform films of wax in the dimensions of the PDMS trench. Similar procedures formed uniform spacer layers of wax (outer dimensions, 2 cm × 2 cm; inner dimensions, 1 cm × 1 cm; thickness, 100 µm). Two uniform films of wax sandwiched the eb-MEMS with the wax spacer in the middle. Slightly melting the edges of these wax films enabled strong bonding at the interface.

Hydrogel packaging for contacting-type eb-MEMS. Fabrication processing.

Anchoring a PLA capping structure (2 mm × 2 mm × 200 µm) formed by 3D printing with four circular holes (diameter, 600 µm) above the eb-MEMS device prevented direct contact between the device and the hydrogel. Synthesis of the hydrogel followed the steps described in a previous study⁶¹, beginning with the formation of two solutions (Solution I and Solution II). Solution I (pH 7.0) consisted of bifunctional PEG-LA-DA macromers (40.0 wt%), Irgacure D-2959 (0.4 wt%) and CaCl₂ (0.5 wt%) in ultrapure water. Solution II (pH 7.0) contained sodium alginate (5.0 wt%) in ultrapure water. Bubbling nitrogen (N₂) gas into these solutions for 10 min and then degassing them for 10 min removed most of the dissolved oxygen (O₂). The primer synthesis followed protocols published in a previous study⁶¹. The process began with dissolving chitosan (2.0 wt%) in 2-(N-morpholino) ethanesulfonic acid buffer (pH 5.0) followed by the addition of carbodiimide reagents (EDC, 0.5 wt%; Sulfo-NHS, 0.5 wt%). The process was complete after spreading the primers and mixing and spreading the hydrogel solutions at a volume ratio of 1:1 with a dual-syringe delivery system onto the eb-MEMS, followed by exposure to UV light (wavelength, 365 nm; density, 20 mW cm⁻²) for 3 min.

Characterizations of hydrogel adhesion to tissues. Experiments involved peeling the hydrogel pieces (50 mm × 25 mm × 2 mm) from the tissue surfaces (50 mm × 25 mm; thickness differs among different tissues). Plastic films (thickness, 50 µm) bonded to the hydrogels and the tissue samples minimized the contribution of elastic energy dissipation to the test results. The peeling rate was 60 mm min⁻¹. Two times the value of the plateau force divided by the width of the specimen yielded the adhesion energy. Peeling and tensile tests were performed by MTS Sintech 20/G (MTS).

Characterizations of protein diffusion. Characterization utilized UV-vis spectroscopy and confocal fluorescence microscopy. For UV-vis spectroscopy, BSA (Sigma-Aldrich) served as a representative protein to characterize protein diffusion in the hydrogel layer (diameter, 3 cm; thickness, 400 µm). The placement of the BSA solution at a higher concentration (0.70 mg ml⁻¹ in PBS; pH 7.4; height, 12.5 µm) above a layer of hydrogel and another BSA solution at a lower concentration (0.25 mg ml⁻¹ in PBS; pH 7.4; height, 12.5 µm) underneath this layer defined the experimental setup, stored at 37 °C and sealed with a paraffin film to prevent water evaporation. Extracting the BSA solution from the top and bottom regions (volume, 100 µl) every 12 h, followed by dilution with PBS (pH 7.4) to a volume of 1 ml enabled measurement by UV-vis absorption (Evolution 201 UV-vis spectrophotometers; Thermo Fisher Scientific). Standard BSA solutions with concentrations from 0.20–1.00 mg ml⁻¹ served as references to establish a calibration curve for the UV-vis absorption data collection. The resulting time dependence of the concentrations of BSA in the solutions above and below the hydrogel provided the basis for determining the diffusivity of BSA through the hydrogel. For confocal fluorescence microscopy, Alexa Fluor 488-conjugate BSA (Thermo Fisher Scientific) served as a representative protein for diffusion measurements. Placing the hydrogel layer (2 cm × 2 cm × 400 µm) at the bottom of a trench formed in a piece of PDMS and then filling the trench with a conjugated BSA solution (0.10 mg ml⁻¹ in PBS; pH 7.4) created a setup for the experiments, stored at 37 °C. Real-time imaging of BSA diffusion into the hydrogel by confocal microscopy (SP8; Leica Microsystems), followed by image analysis (LAX S Life Science; Leica Microsystems) yielded data for determining the diffusion rate.

Characterizations of fragment confinement. Si MMAs served as materials for characterizing the effects of fragment confinement. Fabrication of the Si MMAs began with laser cutting a silicon-on-insulator wafer (top Si layer thickness,

1.5 µm; buried SiO₂ thickness, 1 µm; substrate thickness, 675 µm; Soitec) into small square pieces (5 mm × 5 mm). Immersing these pieces into HF (concentration, 49%) for 48 h yielded Si MMAs, subsequently retrieved using a customized plastic pipette and rinsed with IPA and DI water. Placing the Si MMAs at the bottom of a quartz cuvette (interior dimensions, 10 mm × 10 mm) allowed them to be covered with a layer of hydrogel (dimensions, 10 mm × 10 mm × 400 µm) bonded to the bottom surface of the cuvette. Filling the cuvette with PBS (pH 7.4) and placing the experimental setup in an oven at 37 °C completed the process.

Cell-based assays of mechanotransduction and effects of MP or TP extract media.

Cell culture. CAF05 human colon fibroblasts (Neuromics) were precultured in Vitroplus III, low-serum, complete medium (Neuromics) and incubated at 37 °C in a humidified atmosphere with 5% CO₂. Preparation of the MP and TP extract media involved dissolving MP or TP deposited on both sides of a silicon wafer (thickness, 600 nm for MP and 2 µm for TP; dimensions, 5 cm × 2 cm; quantity, ~10) by immersion in a PTFE bottle filled with PBS (pH 7.4; volume, ~20 ml) at 85 °C for seven days, created PBS solution conditioned with dissolved MP or TP. Analysis through ICP-OES (iCAP 7600; Thermo Fisher Scientific) yielded the concentrations of the extracts. Diluting solutions with additional culture media enabled the desired extract concentrations for tests (concentration for each, 1.0 mM). Culturing the cells in the conditioned media at 37 °C allowed characterization of the effect of dissolved MP/TP extracts on the cells for 12 h.

In situ characterization of cell–extracellular matrix mechanotransduction.

Polyacrylamide (PAAm) hydrogel substrates for traction force microscopy (TFM) characterization were prepared following previously reported protocols⁶². The synthesis of PAAm hydrogels on sterilized glass-bottom dishes involved silanizing the bottom glass with (3-aminopropyl)trimethoxysilane (Sigma-Aldrich) and functionalizing with glutaraldehyde (0.5 vol%; Polysciences) to facilitate the attachment of the PAAm hydrogel. A mixture of acrylamide (40%; Sigma-Aldrich), N,N'-methylenebisacrylamide (2 vol%; Sigma-Aldrich) and PBS (pH 7.4) was then used to generate a liquid hydrogel precursor solution to polymerize into a hydrogel of ~5 kPa elastic modulus. Ammonium persulfate (1.0 vol%; Bio-Rad Laboratories) and tetramethylethylenediamine (0.1 vol%; Bio-Rad Laboratories) catalysed the polymerization reaction. Embedding the hydrogels with fiducial beads close to the top surface followed the previously described protocol⁶³. Treating the glass coverslips by poly-D-lysine (PDL; 0.1 mg ml⁻¹; Sigma-Aldrich) for 1 h enhanced the attachment of the dark-red fluorescent beads (excitation/emission wavelength, 660/680 nm; diameter, 200 nm; Thermo Fisher Scientific). These beads allowed the tracking of cell traction over extended periods of time without inducing photosensitivity in the cells⁶⁴. Diluting the stock colloid suspension of the beads with DI water at a ratio of 1:5,000, followed by pipetting onto the PDL-coated coverslips for 10 min allowed these beads to settle onto the surface of the substrate. The coverslips were blow dried and placed on the liquid PAAm gel-coated samples during gel polymerization, thereby uniformly embedding the beads into the liquid PAAm hydrogel via gravity-driven diffusion. The coverslips were then peeled off, and the hydrogels were treated with sulfosuccinimidyl-6-(4'-azido-2'-nitrophenylamino)-hexanoate (0.02 vol%; Thermo Fisher Scientific) in 4-(2-hydroxyethyl)-1-piperazineethanesulfonic acid (HEPES) buffer (50 mM, pH 8.5; Thermo Fisher Scientific) with UV activation for 15 min. Immersing the hydrogel substrates in a fibronectin solution (human, 25 µg ml⁻¹; Corning) in HEPES buffer overnight functionalized the extracellular matrix and subsequently rinsed with PBS (pH 7.4). The CAF05 fibroblasts were exposed to the conditioned media (1 mM extracts from the eb-MEMS) after 4 h of seeding following attachment and spreading on the TFM substrate. Phase-contrast and fluorescent images of the cells and fiducial beads were obtained every 30 min for 12 h. At the end of the experiment, the cells were lysed with 1% sodium dodecyl sulfate, and reference (undeformed configuration) bead images were acquired.

Evaluation of cytocompatibility of MP and TP layers in vitro. Maintaining and culturing a mouse fibroblast cell line (CCL-1; ATCC) occurred in culture flasks (surface area, 25 cm²) filled with cell media (30–2003; ATCC). The viability assay utilized the cells after the second subculture. Exposure to ethylene oxide gas (AN74i sterilizer; Andersen) sterilized the silicon wafers coated with MP and TP (1 cm × 1 cm). Placing the samples into the cell culture plate (Corning), followed by seeding the cells above these samples at a concentration of 10,000 cells ml⁻¹, prepared the system for characterization. After maintaining the cells for 24 h, staining with a live/dead viability/cytotoxicity kit (L3224; Thermo Fisher Scientific) according to the manufacturer's protocols allowed the quantitative evaluations of the cytocompatibility of MP and TP layers.

Sterile processes for animal studies. Exposure to ethylene oxide gas (AN74i sterilizer) sterilized the eb-MEMS devices. The sterilization process for the hydrogel followed the steps described previously⁶¹. Briefly, dissolving microfiltered and lyophilized sodium alginate and high-purity chitosan in ultrapure water (0.5 wt%), followed by sterile filtering (220-nm-diameter membrane pores), freezing at -20 °C for 3 h and then lyophilizing for 6 h completed the process. Other chemicals (PEG-LA-DA, CaCl₂, Irgacure D-2959, EDC and Sulfo-NHS) followed the filtering sterilization procedure (220-nm-diameter membrane pores)

immediately before use. External equipment, including surgical tools, adaptors, UV lamps and readout machines, were wiped with pieces of cloth soaked in ethanol (75 vol%).

Evaluation of biocompatibility in vivo. Biocompatibility studies in animals followed protocols approved by the Institutional Animal Care and Use Committee at Northwestern University and in accordance with the Guide for the Care and Use of Laboratory Animals. All the procedures were performed under general anaesthesia using isoflurane. Male Lewis rats weighing 250–350 g (Charles River Laboratories) received subcutaneous injections of buprenorphine hydrochloride (0.05 mg kg⁻¹; Reckitt Benckiser) for pain management and ampicillin (50 mg kg⁻¹; Sage Therapeutics) to prevent infection at the implantation site before the surgical process. Forming a 1-cm-long incision over the shaved back exposed the dorsal subcutaneous tissues. Placing the eb-MEMS device on the subcutaneous tissue, followed by spreading primers and adhesive precursors, and applying UV exposure completed the implantation process. Euthanasia of the rats after 28 days of implantation enabled the explantation of organs, including the brain, heart, kidneys, liver, lung, spleen and skin, as well as the extraction of blood for further biocompatibility studies. For histological analysis, the organs were fixed in formalin (concentration, 10 vol%), followed by embedding in paraffin, sectioning and staining with H&E. For haematology and blood chemistry, collecting blood in K-EDTA tubes and gel tubes prepared samples for complete blood counts and blood chemistry tests, performed by Charles River Laboratories.

Evaluation of fragment confinement in vivo. *Surgical procedures.* The fragment studies in animals followed protocols approved by the Institutional Animal Care and Use Committee at Northwestern University and in accordance with the Guide for the Care and Use of Laboratory Animals. Young adult male and female mice (post-natal period, 60–80 days; weight, ~20 g) were used, with an approximately equal number of males and females. These mice received isoflurane (induction value, 3 vol%; maintenance value, 1.5–2.0 vol%) for anaesthesia and ketoprofen (5 mg kg⁻¹) for analgesia, and were placed on a small animal stereotaxic frame (David Kopf Instruments) for the surgery. Puralube vet ointment (Dechra Veterinary Products) covered the eyes of mice during this procedure. Forming a 1-cm-long incision over the shaved back exposed the dorsal subcutaneous tissues. Placing the eb-MEMS device on the subcutaneous tissue, followed by spreading primers and adhesive precursors and exposing them to UV light, completed the implantation process. Implanting the eb-MEMS without the hydrogel layer formed the basis for a comparison group. Nylon 6-0 monofilament (Ethicon) sutures closed the surgical incisions, with standard post-surgical recovery procedures.

Fragment distribution by microCT imaging. MicroCT imaging performed on different post-surgical days determined the distribution of fragments from the eb-MEMS devices. Mice received isoflurane (3 vol% in oxygen) in an induction chamber and were then transferred to a dedicated imaging bed with isoflurane delivered via a nosecone at 1–2 vol%. Each mouse was in the prone position in a dedicated chamber with the head immobilized using ear and tooth bars. The respiratory signals were tracked using a digital monitoring system (Mediso-USA). Image acquisition was done using a preclinical microPET/CT imaging system (Mediso-USA) at 2.17 magnification, 33-μm-diameter focal spot, 1×1 binning, 70 kV_p with 720 projection views over a full circle and 300 ms exposure time. Reconstructing the projection data with a voxel size of 68 μm using filtered (Butterworth filter) back-projection software (Mediso-USA) and visualizing the reconstructed data in Amira v2020.3 (FEI) completed the microCT image analysis. Manually registering the microCT images eliminated artifacts caused by the device.

Measurement of fragment spreading. Analysis used Amira v2020.3 (FEI). MicroCT scans, modified using a non-local means filter, segmented the device and fragments at each timepoint (days 3, 17 and 31 post-surgery) with a combination of thresholding and manual inspection. Cropping the skeleton of the mouse, segmented using a threshold of 700 Hounsfield units, resulted in a region of interest containing only L3, L4 and L5. Automatically registering the vertebral segments from the second and third timepoints to that from the first timepoint utilized normalized mutual information. Copying each vertebral transform to its corresponding device ensured that all the devices registered to the vertebrae from the first timepoint. The device regions of interest were binarized using an automated adaptive thresholding tool, noting the centroid of each device.

Biodistribution by organ analysis. Euthanasia of the mice on day 31 post-surgery enabled the extraction of blood, and explantation and weighing of organs, including the brain, spleen, lung, heart, kidneys, skin and liver. Dissolving the organs and serums with a mixture of 1.50 ml nitric acid (HNO₃) and 0.35 ml hydrogen peroxide (H₂O₂) in preweighed 15 ml conical metal-free tubes, followed by dilution with ultrapure water at a ratio of 1:10 finished the sample preparation. Analysis through ICP-OES (iCAP 7600) and ICP-MS (iCAP Q; Thermo Fisher Scientific) yielded the concentration of Si and Mo, respectively, in the organs at day 31 post-surgery. The concentrations of these elements determined the biodistribution and biodegradability of dissolved Si and Mo from the eb-MEMS and excess fragments.

Statistical analysis. Statistical significance and *p* values (Fig. 3f,g and Supplementary Fig. 22d–f) are determined by one-way analysis of variance using GraphPad Prism software. The significance thresholds were **p*<0.05, ***p*<0.01 and ****p*<0.001. Here ns indicates no statistically significant differences.

Reporting summary. Further information on research design is available in the Nature Research Reporting Summary linked to this article.

Data availability

The data that support the findings of this study are available from the corresponding author upon reasonable request.

Received: 13 July 2021; Accepted: 7 June 2022;
Published online: 21 July 2022

References

- Ni, X. et al. Automated, multiparametric monitoring of respiratory biomarkers and vital signs in clinical and home settings for COVID-19 patients. *Proc. Natl Acad. Sci. USA* **118**, e2026610118 (2021).
- Lee, K. et al. Mechano-acoustic sensing of physiological processes and body motions via a soft wireless device placed at the suprasternal notch. *Nat. Biomed. Eng.* **4**, 148–158 (2020).
- del Rosario, M., Redmond, S. & Lovell, N. Tracking the evolution of smartphone sensing for monitoring human movement. *Sensors* **15**, 18901–18933 (2015).
- Brigante, C. M. N., Abbate, N., Basile, A., Faulisi, A. C. & Sessa, S. Towards miniaturization of a MEMS-based wearable motion capture system. *IEEE Trans. Ind. Electron.* **58**, 3234–3241 (2011).
- Shasha Liu, P. & Tse, H.-F. Implantable sensors for heart failure monitoring. *J. Arrhythmia* **29**, 314–319 (2013).
- Mohd Ghazali, F. A. et al. MEMS actuators for biomedical applications: a review. *J. Micromech. Microeng.* **30**, 073001 (2020).
- Potekhina, A. & Wang, C. Review of electrothermal actuators and applications. *Actuators* **8**, 69 (2019).
- Zhao, C. et al. A review on coupled MEMS resonators for sensing applications utilizing mode localization. *Sens. Actuators A* **249**, 93–111 (2016).
- Totsu, K., Moriyama, M. & Esashi, M. MEMS research is better together. *Nat. Electron.* **2**, 134–136 (2019).
- Han, C.-H. et al. MEMS packaging method without any heating or external force using adhesive bonding assisted by capillary force. In *2017 19th International Conference on Solid-State Sensors, Actuators and Microsystems (TRANSDUCERS)* 1221–1224 (IEEE, 2017).
- Imboden, M. et al. Building a fab on a chip. *Nanoscale* **6**, 5049–5062 (2014).
- Guo, R., Xu, R., Wang, Z., Sui, F. & Lin, L. Accelerating MEMS design process through machine learning from pixelated binary images. In *2021 IEEE 34th International Conference on Micro Electro Mechanical Systems (MEMS)* 153–156 (IEEE, 2021).
- Dieseldorff, C. G. & Clark, T. *MEMS & Sensors Fab Report to 2023* (2019).
- O'Dea, S. Number of smartphones sold to end users worldwide from 2007 to 2021. *Gartner* <https://www.statista.com/statistics/263437/global-smartphone-sales-to-end-users-since-2007/> (2021).
- Scansen, D. How MEMS enable smartphone features. *Engineering.com* <https://www.engineering.com/story/how-mems-enable-smartphone-features> (2013).
- Awasthi, A. K., Li, J., Koh, L. & Ogunseitan, O. A. Circular economy and electronic waste. *Nat. Electron.* **2**, 86–89 (2019).
- Fu, J., Zhang, H., Zhang, A. & Jiang, G. E-waste recycling in China: a challenging field. *Environ. Sci. Technol.* **52**, 6727–6728 (2018).
- Althaif, S., Babbitt, C. W. & Chen, R. Forecasting electronic waste flows for effective circular economy planning. *Resour. Conserv. Recycl.* **151**, 104362 (2019).
- Jambeck, J. R. et al. Plastic waste inputs from land into the ocean. *Science* **347**, 768–771 (2015).
- Electronic waste—our greatest threat. *Recycle magazine* <https://www.recyclingmagazine.com/2021/02/25/electronic-waste-our-greatest-threat/> (2021).
- Irimia-Vladu, M. et al. Green and biodegradable electronics. *Mater. Today* **15**, 340–346 (2012).
- Williams, N. X., Bullard, G., Brooke, N., Therien, M. J. & Franklin, A. D. Printable and recyclable carbon electronics using crystalline nanocellulose dielectrics. *Nat. Electron.* **4**, 261–268 (2021).
- Hall-Stoodley, L., Costerton, J. W. & Stoodley, P. Bacterial biofilms: from the natural environment to infectious diseases. *Nat. Rev. Microbiol.* **2**, 95–108 (2004).
- Maytin, M. & Epstein, L. M. Lead extraction is preferred for lead revisions and system upgrades: when less is more. *Circ. Arrhythm. Electrophysiol.* **3**, 413–424 (2010).

25. Boutry, C. M. et al. Towards biodegradable wireless implants. *Philos. Trans. R. Soc. A* **370**, 2418–2432 (2012).
26. Li, C. et al. Design of biodegradable, implantable devices towards clinical translation. *Nat. Rev. Mater.* **5**, 61–81 (2020).
27. Peroulis, D. et al. CMOS MEMS fabrication technologies. In *Encyclopedia of Nanotechnology* 441–449 (Springer, 2012).
28. Baltes, H., Brand, O., Hierlemann, A., Lange, D. & Hagleitner, C. CMOS MEMS—present and future. In *Technical Digest. MEMS 2002 IEEE International Conference. Fifteenth IEEE International Conference on Micro Electro Mechanical Systems (Cat. No.02CH37266)* 459–466 (IEEE, 2002).
29. Bettinger, C. J., Bruggeman, J. P., Misra, A., Borenstein, J. T. & Langer, R. Biocompatibility of biodegradable semiconducting melanin films for nerve tissue engineering. *Biomaterials* **30**, 3050–3057 (2009).
30. Boutry, C. M. et al. A stretchable and biodegradable strain and pressure sensor for orthopaedic application. *Nat. Electron.* **1**, 314–321 (2018).
31. Jung, Y. H., Zhang, H., Gong, S. & Ma, Z. High-performance green semiconductor devices: materials, designs, and fabrication. *Semicond. Sci. Technol.* **32**, 063002 (2017).
32. Cao, J. & Nguyen, C. T.-C. Drive amplitude dependence of micromechanical resonator series motional resistance. In *10th International Conference on Solid-State Sensors and Actuators* 1826–1829 (1999).
33. Kaajakari, V., Koskinen, J. K. & Mattila, T. Phase noise in capacitively coupled micromechanical oscillators. *IEEE Trans. Ultrason., Ferroelectr., Freq. Control* **52**, 2322–2331 (2005).
34. Lu, X. et al. Extreme strain rate and temperature dependence of the mechanical properties of nano silicon nitride thin layers in a basal plane under tension: a molecular dynamics study. *Phys. Chem. Chem. Phys.* **16**, 15551–15557 (2014).
35. Heinisch, M., Voglhuber-Brunnmaier, T., Reichel, E. K., Dufour, I. & Jakoby, B. Reduced order models for resonant viscosity and mass density sensors. *Sens. Actuators A* **220**, 76–84 (2014).
36. Cerimovic, S. et al. Sensing viscosity and density of glycerol–water mixtures utilizing a suspended plate MEMS resonator. *Microsyst. Technol.* **18**, 1045–1056 (2012).
37. Yin, L. et al. Mechanisms for hydrolysis of silicon nanomembranes as used in bioresorbable electronics. *Adv. Mater.* **27**, 1857–1864 (2015).
38. Kang, S.-K. et al. Biodegradable thin metal foils and spin-on glass materials for transient electronics. *Adv. Funct. Mater.* **25**, 1789–1797 (2015).
39. Choi, Y. S. et al. Biodegradable polyanhydrides as encapsulation layers for transient electronics. *Adv. Funct. Mater.* **30**, 2000941 (2020).
40. Chang, J.-K. et al. Cytotoxicity and in vitro degradation kinetics of foundry-compatible semiconductor nanomembranes and electronic microcomponents. *ACS Nano* **12**, 9721–9732 (2018).
41. Vetter, R. J., Williams, J. C., Hetke, J. F., Nunamaker, E. A. & Kipke, D. R. Chronic neural recording using silicon-substrate microelectrode arrays implanted in cerebral cortex. *IEEE Trans. Biomed. Eng.* **51**, 896–904 (2004).
42. Shin, J. et al. Bioresorbable pressure sensors protected with thermally grown silicon dioxide for the monitoring of chronic diseases and healing processes. *Nat. Biomed. Eng.* **3**, 37–46 (2019).
43. Lange, J. R. & Fabry, B. Cell and tissue mechanics in cell migration. *Exp. Cell Res.* **319**, 2418–2423 (2013).
44. Canović, E. P., Zollinger, A. J., Tam, S. N., Smith, M. L. & Stamenović, D. Tensional homeostasis in endothelial cells is a multicellular phenomenon. *Am. J. Physiol. Cell Physiol.* **311**, C528–C535 (2016).
45. Bellas, E. & Chen, C. S. Forms, forces, and stem cell fate. *Curr. Opin. Cell Biol.* **31**, 92–97 (2014).
46. Taylor-Weiner, H., Ravi, N. & Engler, A. J. Traction forces mediated by integrin signaling are necessary for definitive endoderm specification. *J. Cell Sci.* **128**, 1961–1968 (2015).
47. Li, B. & Wang, J. H.-C. Fibroblasts and myofibroblasts in wound healing: force generation and measurement. *J. Tissue Viability* **20**, 108–120 (2011).
48. Emon, B., Bauer, J., Jain, Y., Jung, B. & Saif, T. Biophysics of tumor microenvironment and cancer metastasis—a mini review. *Computational Struct. Biotechnol. J.* **16**, 279–287 (2018).
49. Bauer, J. et al. Increased stiffness of the tumor microenvironment in colon cancer stimulates cancer associated fibroblast-mediated prometastatic activin A signaling. *Sci. Rep.* **10**, 50 (2020).
50. Guertin, D. A. & Sabatini, D. M. Cell size control. In *Encyclopedia of Life Sciences* (John Wiley & Sons, 2006).
51. Li, J. K.-J. *Dynamics of the Vascular System: Interaction with the Heart* (World Scientific, 2018).
52. Yang, Q., Hu, Z. & Rogers, J. A. Functional hydrogel interface materials for advanced bioelectronic devices. *Acc. Mater. Res.* **2**, 1010–1023 (2021).
53. Yang, Q. et al. Materials, mechanics designs, and bioresorbable multisensor platforms for pressure monitoring in the intracranial space. *Adv. Funct. Mater.* **30**, 1910718 (2020).
54. Hettiaratchi, M. H. et al. A rapid method for determining protein diffusion through hydrogels for regenerative medicine applications. *APL Bioeng.* **2**, 026110 (2018).
55. Leach, J. B. & Schmidt, C. E. Characterization of protein release from photocrosslinkable hyaluronic acid–polyethylene glycol hydrogel tissue engineering scaffolds. *Biomaterials* **26**, 125–135 (2005).
56. Chakraborty, R. et al. Association of body length with ocular parameters in mice. *Optom. Vis. Sci.* **94**, 387–394 (2017).
57. Chang, J.-K. et al. Materials and processing approaches for foundry-compatible transient electronics. *Proc. Natl Acad. Sci. USA* **114**, E5522–E5529 (2017).
58. Chang, J.-K. et al. Biodegradable electronic systems in 3D, heterogeneously integrated formats. *Adv. Mater.* **30**, 1704955 (2018).
59. Schneider, C. A., Rasband, W. S. & Eliceiri, K. W. NIH image to Image: 25 years of image analysis. *Nat. Methods* **9**, 671–675 (2012).
60. Schindelin, J. et al. Fiji: an open-source platform for biological-image analysis. *Nat. Methods* **9**, 676–682 (2012).
61. Yang, Q. et al. Photocurable bioresorbable adhesives as functional interfaces between flexible bioelectronic devices and soft biological tissues. *Nat. Mater.* **20**, 1559–1570 (2021).
62. Tse, J. R. & Engler, A. J. Preparation of hydrogel substrates with tunable mechanical properties. *Curr. Protoc. Cell Biol.* **47**, 10.16.1–10.16.16 (2010).
63. Knoll, S. G., Ali, M. Y. & Saif, M. T. A. A novel method for localizing reporter fluorescent beads near the cell culture surface for traction force microscopy. *J. Vis. Exp.* **91**, e51873 (2014).
64. Emon, M. A. B. et al. Dose-independent threshold illumination for non-invasive time-lapse fluorescence imaging of live cells. *Extrem. Mech. Lett.* **46**, 101249 (2021).

Acknowledgements

This work was supported by the Querry Simpson Institute for Bioelectronics at Northwestern University. We especially thank L. Saggere at the University of Illinois Chicago for helping with the optical characterization of the devices. This work made use of the NUFAB facility of Northwestern University's NUANCE Center, which has received support from the Soft and Hybrid Nanotechnology Experimental (SHyNE) Resource (NSF ECCS-2025633); the MRSEC program (NSF DMR-1720139) at the Materials Research Center; the International Institute for Nanotechnology (IIN); the Keck Foundation; the Querry Simpson Institute for Bioelectronics; the Keck Biophysics Facility, a shared resource of the Robert H. Lurie Comprehensive Cancer Center of Northwestern University, which has received support in part by the NCI Cancer Center Support (P30 CA060553); the Center for Advanced Molecular Imaging (RRID:SCR_021192); Northwestern University; and the State of Illinois, through the IIN. Elemental analysis was performed at the Northwestern University Quantitative Bio-element Imaging Center generously supported by NASA Ames Research Center Grant (NNA04CC36G). B.E. acknowledges support from the National Institutes of Health (T32 EB019944). M.W. acknowledges support from the National Institutes of Health (T32 AG20506). Y.K. acknowledges support from the National Institutes of Health (R01 NS107539 and R01 MH117111), Beckman Young Investigator Award, Rita Allen Foundation Scholar Award and Searle Scholar Award. M.T.A.S. acknowledges support from the National Science Foundation (ECCS 19-34991) and Illinois Cancer Center seed grant at the University of Illinois at Urbana-Champaign. Y.H. acknowledges support from the National Science Foundation (CMMI 16-35443). The diagrams in Figs. 4a and 5a are created with BioRender (<https://biorender.com/>).

Author contributions

Q.Y., J.-K.C. and J.A.R. conceived the ideas and designed the research. Q.Y., T.-L.L., Y. Xue and Y.C. designed the devices. Q.Y., T.-L.L., Y. Xu, C.R., T.W., C.C., Z.H., C.W., M.H. and J.M.T. fabricated and characterized the devices. Y. Xue, H.W. and Y.H. performed the numerical simulations. B.E., M.W., I.K., C.R.H., A.B., I.S., J.H., R.A.S., L.L., Y.K. and M.T.A.S. performed the in vitro and in vivo studies. Q.Y., T.-L.L., Y. Xu, B.E., C.R., T.W. and J.H. performed the data analysis. Q.Y., J.-K.C. and J.A.R. wrote the manuscript with input from all the authors.

Competing interests

The authors declare no competing interests.

Additional information

Supplementary information The online version contains supplementary material available at <https://doi.org/10.1038/s41928-022-00791-1>.

Correspondence and requests for materials should be addressed to Jan-Kai Chang or John A. Rogers.

Peer review information *Nature Electronics* thanks Christopher Bettinger, Roozbeh Tabrizian and the other, anonymous, reviewer(s) for their contribution to the peer review of this work.

Reprints and permissions information is available at www.nature.com/reprints.

Publisher's note Springer Nature remains neutral with regard to jurisdictional claims in published maps and institutional affiliations.

© The Author(s), under exclusive licence to Springer Nature Limited 2022

Reporting Summary

Nature Research wishes to improve the reproducibility of the work that we publish. This form provides structure for consistency and transparency in reporting. For further information on Nature Research policies, see our [Editorial Policies](#) and the [Editorial Policy Checklist](#).

Statistics

For all statistical analyses, confirm that the following items are present in the figure legend, table legend, main text, or Methods section.

n/a Confirmed

- The exact sample size (n) for each experimental group/condition, given as a discrete number and unit of measurement
- A statement on whether measurements were taken from distinct samples or whether the same sample was measured repeatedly
- The statistical test(s) used AND whether they are one- or two-sided
Only common tests should be described solely by name; describe more complex techniques in the Methods section.
- A description of all covariates tested
- A description of any assumptions or corrections, such as tests of normality and adjustment for multiple comparisons
- A full description of the statistical parameters including central tendency (e.g. means) or other basic estimates (e.g. regression coefficient) AND variation (e.g. standard deviation) or associated estimates of uncertainty (e.g. confidence intervals)
- For null hypothesis testing, the test statistic (e.g. F , t , r) with confidence intervals, effect sizes, degrees of freedom and P value noted
Give P values as exact values whenever suitable.
- For Bayesian analysis, information on the choice of priors and Markov chain Monte Carlo settings
- For hierarchical and complex designs, identification of the appropriate level for tests and full reporting of outcomes
- Estimates of effect sizes (e.g. Cohen's d , Pearson's r), indicating how they were calculated

Our web collection on [statistics for biologists](#) contains articles on many of the points above.

Software and code

Policy information about [availability of computer code](#)

Data collection

- Fig. 2b, Fig. 4b, and Supplementary Fig. 12 used an oscilloscope system (SIGLENT Technologies).
- Fig. 2d,e,g,h and Supplementary Fig. 17 used a spectrum analyzer system (Rigol Technologies) or MSV 400 series microscope scanning vibrometer system (Polytec, Inc.).
- Fig. 2j used VHX-6000 series digital microscope system (Keyence).
- Fig. 2k used micro-radiometric thermal imaging microscope system (Optotherm).
- Fig. 3a-c used OLS5000 3D laser confocal microscope (Olympus).
- Fig. 3f-g and Supplementary Fig. 22 used IX81 microscope system (Olympus).
- Fig. 4d used Sintech 20G system (MTG).
- Fig. 4e and Supplementary Fig. 28 used Evolution 201 UV-Visible spectrophotometer system (Thermo Fisher Scientific).
- Fig. 5h used microCT digital monitoring system (Mediso-USA).
- Fig. 5i used iCAP 7600 inductively coupled plasma optical emission spectrometry system (Thermo Fisher Scientific).
- Fig. 5j used iCAP Q inductively coupled plasma mass spectrometry system (Thermo Fisher Scientific).
- Supplementary Fig. 23 used Olympus VS120 system (Olympus Corporation).

Data analysis

Fig. 2d,e,g,h and Supplementary Fig. 17 were analyzed by Matlab R2016b software (MathWorks).
 Fig. 2f and Supplementary Fig. 6d-f, 7c-d, 12, 14, 15, 16, 17 were analyzed by ABAQUS Analysis 2010 V6.10 software (Simulia) and COMSOL Multiphysics v5.2a software (COMSOL, Inc.).
 Fig. 2j, Fig. 3f-g, and Supplementary Fig. 22 were analyzed by FIJI (ImageJ 1.52p, Schindelin et al., 2012).
 Fig. 5f-h and Supplementary Fig. 31 were reconstructed by filtered (Butterworth filter) back-projection software from Mediso and visualized in Amira 6.7. The microCT results were analyzed using Amira 6.2 software (FEI).
 Supplementary Fig. 25 was analyzed by Charles River Laboratories.

For manuscripts utilizing custom algorithms or software that are central to the research but not yet described in published literature, software must be made available to editors and reviewers. We strongly encourage code deposition in a community repository (e.g. GitHub). See the Nature Research [guidelines for submitting code & software](#) for further information.

Data

Policy information about [availability of data](#)

All manuscripts must include a [data availability statement](#). This statement should provide the following information, where applicable:

- Accession codes, unique identifiers, or web links for publicly available datasets
- A list of figures that have associated raw data
- A description of any restrictions on data availability

The underlying data that supports the findings of this study are available from the corresponding author upon reasonable request.

Field-specific reporting

Please select the one below that is the best fit for your research. If you are not sure, read the appropriate sections before making your selection.

Life sciences Behavioural & social sciences Ecological, evolutionary & environmental sciences

For a reference copy of the document with all sections, see nature.com/documents/nr-reporting-summary-flat.pdf

Life sciences study design

All studies must disclose on these points even when the disclosure is negative.

Sample size

The work was an explorative proof-of-concept; therefore, we did not pre-determine the sample size needed for significance.

Sample size was 8 biologically independent cell samples in Fig. 3f-g and Supplementary Fig. 22.

Sample size was 3 biologically independent animals in Fig. 3h and Supplementary Fig. 24.

Sample size was 3 biologically independent animals in w/o and w HAM groups, and was 2 biologically independent animals in control group in Fig. 5h-j.

Sample size was 4 biologically independent cell samples in Supplementary Fig. 23.

Sample size was 3 biologically independent animals in Supplementary Fig. 25 and 31.

Statistical significance and P values of Fig. 3f-g and Supplementary Fig. 22d-f are determined by one-way ANOVA.

Data exclusions

The following animals were excluded: Animals that did not survive the surgery. The following cells were excluded: Cells that started differentiation during the measurement.

Replication

All experiments were replicated based on the sample sizes from independent samples and biologically independent animals, perform on separated days.

Randomization

All devices and animals tested were selected randomly.

Blinding

Blinding was not relevant to this work since the metrics are quantified and objectively analyzed.

Reporting for specific materials, systems and methods

We require information from authors about some types of materials, experimental systems and methods used in many studies. Here, indicate whether each material, system or method listed is relevant to your study. If you are not sure if a list item applies to your research, read the appropriate section before selecting a response.

Materials & experimental systems

n/a	Involved in the study
<input checked="" type="checkbox"/>	Antibodies
<input type="checkbox"/>	Eukaryotic cell lines
<input checked="" type="checkbox"/>	Palaeontology and archaeology
<input type="checkbox"/>	Animals and other organisms
<input checked="" type="checkbox"/>	Human research participants
<input checked="" type="checkbox"/>	Clinical data
<input checked="" type="checkbox"/>	Dual use research of concern

Methods

n/a	Involved in the study
<input checked="" type="checkbox"/>	ChIP-seq
<input checked="" type="checkbox"/>	Flow cytometry
<input checked="" type="checkbox"/>	MRI-based neuroimaging

Eukaryotic cell lines

Policy information about [cell lines](#)

Cell line source(s) CAF05 human colon fibroblast cells were purchased from Neuromics (Edina).
CCL-1 mouse fibroblast cells were purchased from ATCC (Manassas).

Authentication Cell lines were authenticated from Neuromics and ATCC.

Mycoplasma contamination Not performed.

Commonly misidentified lines
(See [ICLAC](#) register) No commonly misidentified cell lines were used.

Animals and other organisms

Policy information about [studies involving animals](#); [ARRIVE guidelines](#) recommended for reporting animal research

Laboratory animals	Studies on histology and hematology: Male Lewis rats from Charles River Laboratories weighing 250–350 g at the time of implant. Studies on HAM evaluations: Male and female C57BL/6 mice from Charles River Laboratories weighing ~20 grams, 60–80 days old at the time of implant.
Wild animals	The study did not involve wild animals.
Field-collected samples	This study did not involve samples collected from the field.
Ethics oversight	Biocompatibility studies in animals followed protocols approved by the Institutional Animal Care and Use Committee (IACUC) at Northwestern University and in accordance with the Guide for the Care and Use of Laboratory Animals. HAM studies in animals followed protocols approved by the Institutional Animal Care and Use Committee (IACUC) at Northwestern University and in accordance with the Guide for the Care and Use of Laboratory Animals (protocol #ISO0000707).

Note that full information on the approval of the study protocol must also be provided in the manuscript.